UNIVERSITY OF JYVÄSKYLÄ
DEPARTMENT OF CHEMISTRY

RESEARCH REPORT NO. 157

EERO HULKKO

SPECTROSCOPIC SIGNATURES AS A PROBE OF STRUCTURE AND DYNAMICS IN CONDENSED-PHASE SYSTEMS — STUDIES OF IODINE AND GOLD RANGING FROM ISOLATED MOLECULES TO NANOCLUSTERS

Academic Dissertation for
the Degree of Doctor of Philosophy

UNIVERSITY OF JYVÄSKYLÄ

2012

DEPARTMENT OF CHEMISTRY, UNIVERSITY OF JYVÄSKYLÄ
RESEARCH REPORT No. 157

SPECTROSCOPIC SIGNATURES AS A PROBE OF STRUCTURE AND DYNAMICS IN CONDENSED-PHASE SYSTEMS – STUDIES OF IODINE AND GOLD RANGING FROM ISOLATED MOLECULES TO NANOCLUSTERS

BY

EERO HULKKO

Academic Dissertation
for the Degree of
Doctor of Philosophy

To be presented, by permission of the Faculty of Mathematics and Science of the University of Jyväskylä, for public examination in Auditorium KEM4, on September 14th, 2012 at 12 noon.

UNIVERSITY OF JYVÄSKYLÄ

University of Jyväskylä
Jyväskylä, Finland
ISBN 978-951-39-4839-9
ISSN 0357-346X

URN:ISBN:978-952-86-0175-3
ISBN 978-952-86-0175-3 (PDF)
ISSN 0357-346X

University of Jyväskylä, 2024

ABSTRACT

Hulkko, Eero
Spectroscopic signatures as a probe of structure and dynamics in condensed-phase systems—Studies of iodine and gold ranging from isolated molecules to nanoclusters
Jyväskylä: University of Jyväskylä, 2012, p. 69
(Department of Chemistry, University of Jyväskylä Research Report
ISSN 0357-346X; 157)
ISBN 978-951-39-4839-9
Diss.

This thesis focuses on spectroscopic studies of several different iodine- and gold-containing molecules, complexes and nanoscopic clusters. The systems have been studied in the condensed phase with a wide range of experimental and theoretical techniques.

New spectroscopic signatures have been established for molecular I_2 in solid crystalline Xe and for isolated I_2-Xe-complex in solid Kr by using spectroscopic techniques. The vibrational signatures of several neutral $(I_2)_n$ aggregate complexes in solid Kr have been identified using Resonance Raman spectroscopy. Electronic and vibrational absorption signatures of thiolate-protected gold nanocluster Au_{102}(p-MBA)$_{44}$ have been characterized experimentally from UV-region to far-IR region in solid and liquid phases. Implications of the spectroscopic findings for the dynamical and structural properties of the studied systems have been argued based on density functional calculations and molecular dynamics simulations.

The new experimental results confirm the predicted electronic state structure for the Au_{102}(p-MBA)$_{44}$, and identify the elementary steps of I_2 aggregation toward the crystalline phase. The results establish a novel electronic transition for the weak van der Waals complex I_2-Xe in vacuum-UV absorption and suggest a plausible explanation for the origin. The results also reveal a novel spectroscopic finding of sharp vibronic B↔X structures for condensed-phase I_2. The results open several interesting possibilities for additional studies of these systems.

Keywords: spectroscopy, condensed phase, matrix-isolation, rare gases, iodine, gold, nanoclusters, complexes, dynamics, structure.

Author's address
Eero Hulkko
Nanoscience Center
Department of Chemistry
University of Jyväskylä
P.O. Box 35
FI-40014 University of Jyväskylä
Finland
eero.j.hulkko@jyu.fi

Supervisor
Prof. Mika Pettersson
Nanoscience Center
Department of Chemistry
University of Jyväskylä
P.O. Box 35
FI-40014 University of Jyväskylä
Finland

Reviewers
Prof. Markku Räsänen
Laboratory of Physical Chemistry
Department of Chemistry
University of Helsinki
Finland

Prof. Matti Hotokka
Laboratory of Physical Chemistry
Åbo Akademi University
Finland

Opponent
Dr. Jan Helbing
Institute of Physical Chemistry
University of Zürich
Switzerland

ACKNOWLEDGEMENTS

The work presented in this thesis has been carried out during the years 2008-2012 at the Department of Chemistry at the University of Jyväskylä. Most of the experimental work was done in the laser laboratories of Nanoscience Center. The research has been financially supported by the Academy of Finland and the Department of Chemistry, which are both gratefully acknowledged.

First and foremost, I wish to thank my thesis supervisor Prof. Mika Pettersson for his tireless support during my studies and the preparation of this thesis. I am most thankful for his trust in me, and for all the unique possibilities, scientifically and otherwise, he has given me during these past years. I feel privileged and lucky to have worked under guidance of such an expert and a visionary scientist as Mika truly is. I wish to thank Prof. Hannu Häkkinen for introducing and welcoming us to the intriguing field of gold nanoclusters. I am really grateful for our fruitful collaboration during the last few years. I also wish to thank Prof. Jan Lundell for finding the means to financially support me during the last critical months of this thesis project.

I have had a great fortune to be surrounded by many wonderful, supportive, and most talented people from many fields of natural sciences. I am indeed indebted to many people; without whose efforts I couldn't have finished this project. I want to express my warmest thanks to Doc. Toni Kiljunen whose theoretical calculations, and endless help throughout this project have been crucial for finalizing this thesis. In a sense, Toni has been like a second supervisor of this thesis. I also want to thank especially my dear colleague Dr. Tiina Kiviniemi whose ever-patient guidance and teaching during my first years as a starting scientist, and our collaboration with many publications, have meant great deal to me. I am also very grateful to our in-house collaborators and my other great colleagues: Dr. Jussi Ahokas, Dr. Olga Lopez-Acevedo, Dr. Sami Malola, Dr. Pasi Myllyperkiö, M.Sc. Jaakko Koivisto, and M.Sc. Johan Lindgren for helping and guiding me with the experiments and doing the computational calculations.

I also wish to acknowledge our collaborators from the Stanford Medical School: Prof. Roger Kornberg and Dr. Yael Levi-Kalisman for providing us the beautiful gold nanocluster samples; and Prof. Ara Apkarian from UC Irvine for helping us with the iodine-Xe system. Assistance by Dr. Anders Engdahl with the far-IR instrument in the MAX-LAB facility in Lund is warmly acknowledged. I am also very grateful to the reviewers of this thesis: Prof. Matti Hotokka from Åbo Akademi and Prof. Markku Räsänen from University of Helsinki for their speedy and thorough reading of the manuscript. Their valuable and helpful comments are most warmly appreciated.

Nanoscience Center, with its cornered coffee table at heart of the building, and the old Physical Chemistry building, have always felt like second homes to me. That homely feeling is made by the wonderful people working in these buildings. I want to especially mention my roommate and colleague M.Sc Liisa Antila, for her great friendship, patience, and for our many discussions. I want

to thank all the people from the Nanoscience Center, and especially the people from the Physical Chemistry Department for proving such a unique, homely, and pleasant working environment during these years. I will certainly cherish our common time.

Despite the fact I spent many years away from my old hometown Kokkola; I still seem to have very strong connection to this town. This because many of my oldest friends are still living in Kokkola; or maintain connection to the city. Friends, old and new, you are all dear to me and always in my thoughts. I am thankful for your friendship through all these years.

My heartfelt gratitude goes to my family for their never-ending and unquestionable support: my mother Pirkko, father Antero and my dear siblings Tuomas, Jaakko and Eeva and their wonderful families and spouses. I also want to thank the Harju family for their help and support. Family has always been a safe-haven for me where you could return when most in need.

Lastly, I reserve my deepest gratitude for my own family who have shared all the hardships and the occasional joys through these demanding years – my beloved wife Katja, and our three beautiful sons Henri, Eeli and Aaro, without forgetting You, the one who I haven't really had the pleasure of meeting yet. This work is as much your achievement as it is mine. I could have never done it without your support and love. Kiitos rakkaimmat.

Jyväskylä, August 21th 2012

Eero Hulkko

LIST OF ORIGINAL PUBLICATIONS

The main results in this thesis have been reported in the following publications and they are herein referred by their Roman numerals (I-IV).

I	Hulkko, E.; Lindgren, J.; Kiljunen, T.; Pettersson, M. Long-Lived Electronic Coherence of Iodine in the Condensed Phase: Sharp Zero-Phonon Lines in the B↔X Absorption and Emission of I_2 in Solid Xe, *J. Phys Chem. Lett.* **2012**, *3*, 1847-1852. https://doi.org/10.1021/jz300651v
II	Hulkko, E.; Ahokas, J.; Lindgren, J.; Myllyperkiö, P.; Pettersson, M. Electronic spectroscopy of I_2–Xe complexes in solid Krypton, *J. Chem. Phys.* **2012**, *136*, 174501. https://doi.org/10.1063/1.4706521
III	Hulkko, E.; Kiljunen, T.; Kiviniemi, T.; Pettersson, M. From Monomer to Bulk: Appearance of the Structural Motif of Solid Iodine in Small Clusters, *J. Am. Chem. Soc.* **2009**, *131*, 1050-1056. https://doi.org/10.1021/ja806537u
IV	Hulkko, E.; Lopez-Acevedo, O.; Koivisto, J.; Levi-Kalisman, Y.; Kornberg, R. D.; Pettersson M.; Häkkinen, H. Electronic and Vibrational Signatures of the $Au_{102}(p\text{-MBA})_{44}$ Cluster. *J. Am. Chem. Soc.* **2011**, *133*, 3752-3755. https://doi.org/10.1021/ja111077e

Author's contribution

In Publication I, the Author has done all experimental measurements, analyzed all data, and written the first draft of the publication. In Publication II, the Author has measured and analyzed all time-domain measurements, participated in the absorption measurements, and written the first draft of the publication. In publication III, the Author had a major role in the experimental measurements, analyzed all experimental data, and participated in the calculations, as well as in the writing of the publication. In publication IV, the Author has done most of the experimental measurements and data analysis, including the development of the sample preparation techniques for spectroscopy. The Author has also participated in the writing of the publication.

Other contributions

List of the Author's other publications which are not included in this thesis:

A1. Kiviniemi, T.; Hulkko, E.; Kiljunen, T.; Pettersson, M. Vibrational characterization of the 1:1 Iodine-Benzene Complex isolated in Solid Krypton, *J. Phys. Chem. A* **2008**, *112*, 5025-5027.

A2. Kiviniemi, T.; Hulkko, E.; Kiljunen, T.; Pettersson, M. Iodine-Benzene complex as a candidate for a real-time control of a Bimolecular reaction. Spectroscopic studies of the properties of the 1:1 complex isolated in solid Krypton, *J. Phys. Chem. A* **2009**, *113*, 6326-6333.

A3. Kiviniemi, T.; Hulkko E.; Pettersson, M. Impulsive excitation of high vibrational states in I_2–Xe complex on the electronic ground state, *Chem. Phys. Lett.* **2010**, *491*, 44-48.

A4. Lindgren, J.; Hulkko, E.; Pettersson, M.; Kiljunen, T. Rotational coherence imaging and control for CN molecules through time-frequency resolved coherent anti-Stokes Raman scattering, *J. Chem. Phys.* **2011**, *135*, 224514.

CONTENTS

ABSTRACT
ACKNOWLEDGEMENTS
LIST OF ORIGINAL PUBLICATIONS
CONTENTS
ABBREVIATIONS

1 FOREWORD 13

2 REVIEW OF THE SYSTEMS 16
  2.1 Molecular iodine (I_2) 16
    2.1.1 History and some general properties of iodine 16
    2.1.2 Structure, spectroscopy and dynamics of matrix-isolated I_2 20
  2.2 Complexes of iodine 27
    2.2.1 I_2-Xe 27
    2.2.2 $(I_2)_n$ 29
  2.3 Au_{102}(p-MBA)$_{44}$ 30

3 SOME CONCEPTS OF CONDENSED-PHASE SPECTROSCOPY 35
  3.1 Coherence and dephasing 35
  3.2 Phonon coupling 38

4 METHODOLOGY 40
  4.1 Matrix isolation of I_2 and its complexes 40
  4.2 Gold nanoparticle preparation 42
  4.3 Spectroscopic techniques 43

5 RESULTS AND DISCUSSION 45
  5.1 Signatures of I_2 in solid Xe 45
    5.1.1 Vibronic B↔X ZPLs and PSBs 45
    5.1.2 Long-lived electronic coherence 47
  5.2 Signatures of I_2-Xe complex in solid Kr 48
    5.2.1 VUV absorption and emission 48
    5.2.2 Symmetry breaking of IP states 51
  5.3 Signatures of I_2 clusters in solid Kr 52
    5.3.1 Cluster formation observed by Raman spectroscopy 52
    5.3.2 Structural motif of the crystalline I_2 in small clusters 54
  5.4 Signatures of Au_{102}(p-MBA)$_{44}$ in the condensed phase 55
    5.4.1 Electronic and vibrational signatures 55
    5.4.2 Electronic stability of Au_{102}(p-MBA)$_{44}$ 59

SUMMARY 61

REFERENCES 62

ABBREVIATIONS

CCD	Charge-coupled device
CW	Continuous wave
CT	Charge-transfer
DFT	Density functional theory
DFT-D	DFT with semiempirical dispersion energy correction
DIM	Diatomics-in-molecules
eV	Electron volt
F-C	Franck-Condon
fcc	Face-centered cubic (lattice)
fs	Femtosecond (10^{-15} s)
FTIR	Fourier transform infrared spectroscopy
FWM	Four-wave mixing
GPa	Gigapascal (10^{9} Pa)
GSH	glutathione
HOMO	Highest occupied molecular orbital
ICCD	Image-intensified CCD
IP	Ion-pair
IR	Infrared
LED	Light emitting diode
LIF	Laser-induced fluorescence
LR-TDDFT	Linear-response time-dependent DFT
LUMO	Lowest unoccupied molecular orbital
MCTB	mercury-cadmium-telluride (B-type IR-detector)
Me	Methyl group ($-CH_3$)
MD	Molecular dynamics
MO	Molecular orbital
Nd:YAG	Neodymium:Yttrium Aluminium garnet
NIR	near-IR (typically ≈ 4000-13000 cm^{-1})
NOPA	noncollinear OPA
OPA	Optical parametric amplifier
PAGE	Polyacrylamide gel electrophoresis
p-MBA	Para-mercaptobenzoic acid
PMT	Photomultiplier tube
PSB(s)	Phonon side band(s)
RG(s)	Rare gas(es), usually meaning: Ne, Ar, Kr and Xe
TRCARS	time-resolved coherent anti-Stokes Raman scattering
UV	Ultraviolet, λ_{UV}~< 400 nm
VUV	Vacuum-UV, λ_{VUV}~< 200 nm
ZPL(s)	Zero-phonon line(s)

1 FOREWORD

Spectroscopy deals with the interaction of light (photons) and matter (molecules or atoms), and, more importantly, what such interactions tell us about the matter. Often spectroscopic studies boil down to seeking signatures of matter: clear spectroscopic signs that distinguish, say, a molecule, from another type of molecule, or the same molecule in two different environments. That is the very core theme of this thesis—spectroscopic distinction and definition of simple molecules, molecular complexes, and nanoscopic gold clusters and their environments in the condensed phase. However, the identification of distinctive "bands" in a spectrum (i.e., the spectroscopic signatures) is not the ultimate goal of this thesis, even though such information is sometimes crucial. The important thing is what the signatures can reveal about the structure and the dynamics of the system under study—a fact generally recognized very early on in the development of molecular spectroscopy according to one of the great pioneers in the field, Nobel Laureate Gerhard Herzberg.[1] It goes without saying that the correlations between the observable (spectrum) and the properties of the systems become increasingly difficult to establish as the systems become larger in size just based on the spectroscopic data. Often the only truly fruitful way to proceed is to combine the spectroscopic data with theoretical calculations—another fact emphasized relatively early on by another pioneer in the field, Nobel Laureate Robert Mulliken.[2] Such combined approaches of experimental spectroscopy and theoretical calculations are also adopted in many of the original publications reported in this thesis. The thesis, however, focuses on the experimental results of the publications, for which the Author is mainly responsible. The results from the theoretical work in previous publications will be shown when relevant to the experimental results.

This thesis discusses four original publications (I-IV) of spectroscopic studies of condensed-phase molecular, complex, and thiolate-protected metal cluster systems. The studies range from isolated I_2 molecules[I] through small[II]- and medium[III]-sized iodine complexes to large nanoscopic gold nanoparticles ($Au_{102}(p\text{-}MBA)_{44}$).[IV] The approach adopted in this thesis is to start from the simplest systems, namely the iodine in solid xenon (Xe),[a] and then move on to more complicated systems. The long-lived electronic coherence and the very peculiar nature of I_2 interaction with crystalline solid Xe lattice is dealt with in more detail in publication I, establishing the novel observation of vibronic structures in B↔X absorption and emission of I_2 in the condensed phase. Next, we will look into the spectroscopic signatures of one of the simplest weakly bound van der Waals molecular complexes I_2-Xe, establishing that clear signatures for this bimolecular system can be observed in the vacuum-UV absorption in solid Kr, but, interestingly, not so clearly in the relaxed emission from the ion-pair states. Details of this study can be found in publication II. After this we will move on to more complicated complex systems and to the signatures of neutral iodine clusters $(I_2)_n$, using the Resonance Raman technique in solid Kr. The theme of publication III is the emergence of bulk-like properties in small iodine aggregates. Finally, the thesis examines nanoscopic gold systems. Publication IV establishes the electronic and vibrational signatures for the pure Au_{102}(p-MBA)$_{44}$ gold nanocluster in the condensed phase. The study experimentally establishes the fundamental electronic shell closure and the opening of a HOMO-LUMO band gap for this system. The comparison of the studies from publication I to publication IV emphasizes how spectroscopic observables change when system size increases from small isolated molecules to large and complex systems and from low temperatures to high temperatures. The natural consequence of increasing system complexity and temperature is the spectral broadening of transitions, and the faster loss of coherence, smearing out spectroscopic detail. Nevertheless, important and useful information can be obtained in all cases.

The rest of this thesis is divided into four chapters: 2. *Review of the systems*, 3. *Some concepts of condensed-phase spectroscopy*, 4. *Methodology*, and 5. *Results and discussion*. Chapter 2 provides brief overviews of the four different systems discussed in the four original publications (I-IV). The overview provided in Chapter 2 is not intended as an all-inclusive literary review of the systems and their properties, but merely highlights some properties and previous works that the Author considers interesting and relevant to the results and discussion presented in Chapter 5. A key system in many of the publications (I-III) is the matrix-isolated iodine molecule (I_2). The interaction of "pure" iodine with its environment is the only subject of the study in publication I, but in other cases (II-III) the spectroscopic signatures of the complexes are observed in variance to the spectra of this system. Therefore, the general properties of I_2 are also briefly discussed in Chapter 2. Current research on thiolate-protected gold nanoparticles is moving at a tremendous pace. For example, see the two very recent reviews of the field by Hannu Häkkinen[3] and Rongchao Jin *et al.*[4] Chapter 2 therefore provides only a glimpse of the monolayer-protected gold nanoparticle field with a direct relevance to the Au_{102}(p-MBA)$_{44}$.

Chapter 3 describes qualitatively some key concepts and common phenomena that are important in understanding spectroscopic results in the con-

---

[a] Which is not actually a very simple system at all, as will be shown later on.

densed phase, including the concepts of “coherence” and “dephasing”; there is also a qualitative overview of phonon coupling in crystalline environments. Discussion in Chapter 4 focuses on the technical aspects of the experimental techniques used in the publications: namely the matrix isolation of I_2 and its complexes, and the sample preparation techniques of Au_{102}(p-MBA)$_{44}$. The spectroscopic techniques used in the publications are only briefly mentioned at the end of the chapter. Many of the spectroscopic techniques, such as linear absorption, are reasonably common tools for chemists, and thus the discussion about their properties is mainly technical.

Chapter 5 concludes the thesis by providing an overview of the key results presented in the four original publications. The spectroscopic findings (signatures) are presented first, after which the discussion turns into the significance or possible implications of the results. The chapter merely highlights some of the key results in publications I-IV. For more details, the reader is directed to the four original publications.

2 REVIEW OF THE SYSTEMS

2.1 Molecular iodine (I_2)

2.1.1 History and some general properties of iodine

Iodine is an element of many fascinating properties. The English word *iodine* comes from the Greek word *iōdēs*, meaning "violet-colored" or "violet-like".[5] The English name for the element was originally introduced by Sir Humphry Davy,[6] one of the discoverers of iodine, along with the French chemist Joseph Gay-Lussac.[7] However, credit of isolating iodine in the beginning of the nineteenth century is usually given to the saltpeter manufacturer and chemist Bernard Courtois.[8,9] The name for the heaviest member (M = 126.90 g/mol, Z = 53) of the stable halogens is easy to understand simply by observing the beautiful intense violet color of the iodine vapor.

Generally, the properties of iodine are rather well-known; they can be found in many chemistry textbooks[10] and in Internet sources.[11] Despite the fact that iodine has been under very intense study throughout the past two centuries, and consequently the accumulated literature regarding this system is simply immense, this halogen system still continues to interest the researchers in all fields of natural sciences.[b] The catalytic role of iodine in atmospheric chemistry,[12] high-pressure phases of iodine,[13] properties of iodine in nanoporous materials,[14,15] and supramolecular recognition based on halogen bonding[16] are just few examples of iodine-related research currently of great interest.

In ambient conditions ($T \approx 298.15$ K, $p \approx 1$ bar) elemental iodine (I) exists as a diatomic molecular solid $I_2(s)$,[10] with a notable vapor pressure ($p(I_2) \approx 0.30$ Torr[17]). The schematic crystal structure of solid iodine is depicted in Figure 2-1. Iodine forms layered structures perpendicular to the crystal axis direction *a*.[18,19] The two-dimensional planes in the *b*-*c* axis directions are separated by a dis-

---

[b] For example, a literature review with the word "iodine" on 1. July 2012 in Sciverse Scopus™ reported over 150000 published articles, of which over 2000 just this year.

tance of 4.27 Å (dashed blue line). Within the layers, the I_2 molecules are ordered in zigzag patterns with a shortest intermolecular distance of 3.50 Å (dashed red line). The shortest intermolecular distance in a solid phase is significantly shorter than the van der Waals distance of gas-phase I_2 (R_{wdW} = 3.96 Å).[20, 21] The bond length of I_2 is extended from the gas-phase ground-state value of $R_e(g)$ = 2.666 Å[22] to $R_e(s)$ = 2.715 Å[18] in a crystalline environment. The I_2 crystal has fairly high lattice energy (-63.5 kJ/mol)[23] for a molecular solid, indicating much stronger interactions between the molecules than expected for purely dispersive attraction. The orthorhombic unit cell of solid I_2 contains two iodine atoms and belongs to the C_{mca} space group with D_{2h} symmetry.[24] Iodine has a much higher conductivity within the *b-c* layers than it does perpendicular to the planes.[25] Iodine has a melting point of T_f = 386.8 K and a boiling point of T_b = 458.4 K.[26] The system becomes metallic at a pressure of $p \approx 16$ GPa,[27] and shows a transition from the molecular phase to the monoatomic phase at $p \approx 21$ GPa.[28]

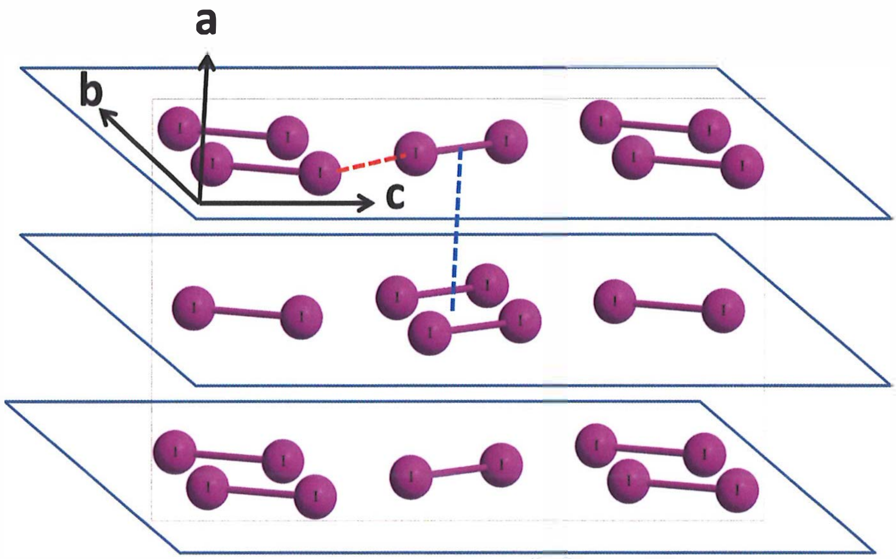

Figure 2-1 The crystal structure of solid I_2. Crystal axis directions (*a,b,c*), shortest intermolecular distance (dashed red line), and the distance between the b-c planes (dashed blue line) are indicated in the figure.

Iodine (I), like other halogen atoms, has a partly filled *p atomic* orbital. The ground-state electronic configuration of atomic I consist of fully occupied inner-core atomic orbitals, identical to a closed-shell Kr atom. The valence consists of fully occupied *5s* valence orbital and partly filled *5p* orbitals ($[Kr]5s^25p^5$). The *molecular* orbital (MO) diagram of iodine molecule (I_2) in the ground electronic configuration is presented in Figure 2-2; in the figure, the innermost fully-occupied MOs have been omitted for clarity. The MO diagram shows how the reasonably weak sigma bond, with a bond dissociation enthalpy $\Delta H^o = 151$ kJ/mol,[26] is formed from the valence electrons in the partially filled *5p* orbitals. The resulting nominal bond order for the ground-state I_2 is therefore one.

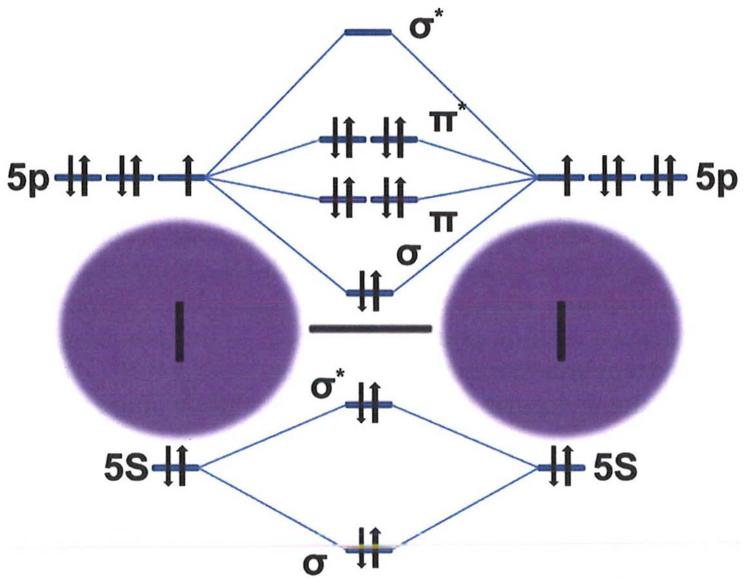

Figure 2-2 Molecular orbital diagram of I_2 in the ground electronic configuration.

The electronic-state structure of iodine, originating from the ground and the excited electronic configurations of the molecule, has received considerable attention in the gas phase, both experimentally[29-36] and theoretically[37,38]. Much of the earlier work on gas-phase iodine has already been reviewed by Mulliken in his publication on the electronic state structure and spectroscopy of iodine.[31] Figure 2-3 shows part of the rather complex electronic-state structure of gas-phase iodine. According to the Mulliken's classification,[31] the neutral electronic states of I_2 can be sorted by their dissociation asymptotes to *valence states* and *ion-pair states* (IP). Iodine has altogether 23 valence states[39] and 20 ion-pair states[35]. The valence states dissociate to two neutral I atoms with electronic term values ^2P ($^2P_{3/2} \equiv I$ or $^2P_{1/2} \equiv I^*$). The valence states dissociate in three distinct asymptotes (I-I, I*-I, I*-I*), which are approximately separated in energy by the spin-orbit splitting of iodine atom (≈ 7600 cm^{-1}).[40] Ten of the valence states, including the ground-state $X(^1\Sigma_g(0_g^+))$, correlate with the lowest dissociation asymptote (I-I). Another set of ten valence states dissociates to the second highest asymptote (I-I*), and three repulsive valence states dissociate to the highest energy limit (I*-I*). The numbers on the right–hand side of Figure 2-3 reflect the total number of electronic states correlating with each of the asymptotes, of which only a few representative and relevant potentials are shown.

The IP states have a different character than the valence states. The 20 IP states correlate to dissociation asymptotes where the dissociation products are ionic: I^- ($^1S_0$) and I^+ ($^1S_0$, $^3P_{0,1,2}$ $^1D_0$). These high-energy states are grouped into three distinct tiers with 6 IP states on each, and one tier with only two states.

Part of the states belonging to the two lowest-energy tiers, the first IP tier (≈ 40000 $\mathrm{cm^{-1}}$) and the second IP tier (≈ 47000 $\mathrm{cm^{-1}}$), are represented in Figure 2-3. The shown IP tiers correlate with the atomic terms $\mathrm{I^-(^1S_0)}$-$\mathrm{I^+(^3P_{0,1,2})}$.[41] In the gas phase, or in symmetrical solvation environments, the IP states are non-polar states because they can be approximately described by symmetrical wavefunctions of the general form:[42]

$$\Psi_{\mathrm{IP,I_2}} \sim \frac{1}{\sqrt{2}}(\Psi_{\mathrm{I^-}}\Psi_{\mathrm{I^+}} \pm \Psi_{\mathrm{I^+}}\Psi_{\mathrm{I^-}}). \tag{2-1}$$

This symmetry of the IP state wavefunctions makes the gas-phase IP states essentially neutral states, similarly to lower-energy valence states of I_2. Electronic transitions of iodine molecule follow to large extent the *Hund's case c* selection rules.[43] In the case of one-photon electronic transitions, the *c*-type selection rules can be written as

$$\Delta\Omega = 0, \pm 1 \tag{2-2}$$

$$u \leftrightarrow g, u \not\leftrightarrow u, g \not\leftrightarrow g \tag{2-3}$$

$$0^+ \leftrightarrow 0^+, 0^- \leftrightarrow 0^-, 0^+ \not\leftrightarrow 0^- \tag{2-4}$$

i.e., the projection of the total angular momentum along the internuclear axis of the molecule $\hbar\Omega$ must remain constant during the electronic transition ($\Delta\Omega = 0$) or differ by one ($\Delta\Omega = \pm 1$). Generally the I_2 transitions with $\Delta\Omega = \pm 1$ are approximately two orders of magnitude weaker than the transitions with $\Delta\Omega = 0$.[33] The inversion symmetry of the electronic wavefunctions through the center of the homonuclear molecule must also change from symmetric (g) to anti-symmetric (u) in an electronic transition. Also the reflection symmetry through a plane containing the internuclear axis in $\Delta\Omega = 0$ transitions must be maintained. For example, the $\mathrm{B(^3\Pi_u(0_u^+))\leftarrow X(^1\Sigma_g(0_g^+))}$ electronic transition, which produces the intense violet color of the I_2(g) molecule, follows these selection rules, even though the strong transition in visible region ($\lambda_{\max} \approx 530$ nm[36]) is not formally allowed by spin-selection rules ($\Delta S = 0$).[43] Despite the fact that the state structure of I_2 is well understood, a rather large number of the 43 electronic states have not been experimentally observed or characterized to date.[34]

As a homonuclear molecule, the I_2 vibration is not IR active. However, the I_2 molecule has been extensively studied using the resonance Raman technique which gives clear vibrational signature for the molecule in different phases.[44-47] Gas-phase iodine (I_2(g)) has a very distinctive Raman active stretch vibration with a fundamental transition energy (G(v=1)-G(v=0)) of 213 $\mathrm{cm^{-1}}$.[22,44] The other extreme in ambient conditions is the bulk solid crystal (I_2(s)). The bulk solid has two Raman active vibrational modes.[47] The vibrational modes of the crystalline

I_2 can be understood as the in-phase vibration (A_g) and the out-of-phase vibration (B_{3g}) of the two I_2 molecules in the orthorhombic unit cell of crystalline I_2.[48] These two modes can be clearly distinguished with their fundamental frequencies at $\omega = 180\ \text{cm}^{-1}$ and $\omega = 189\ \text{cm}^{-1}$, respectively.

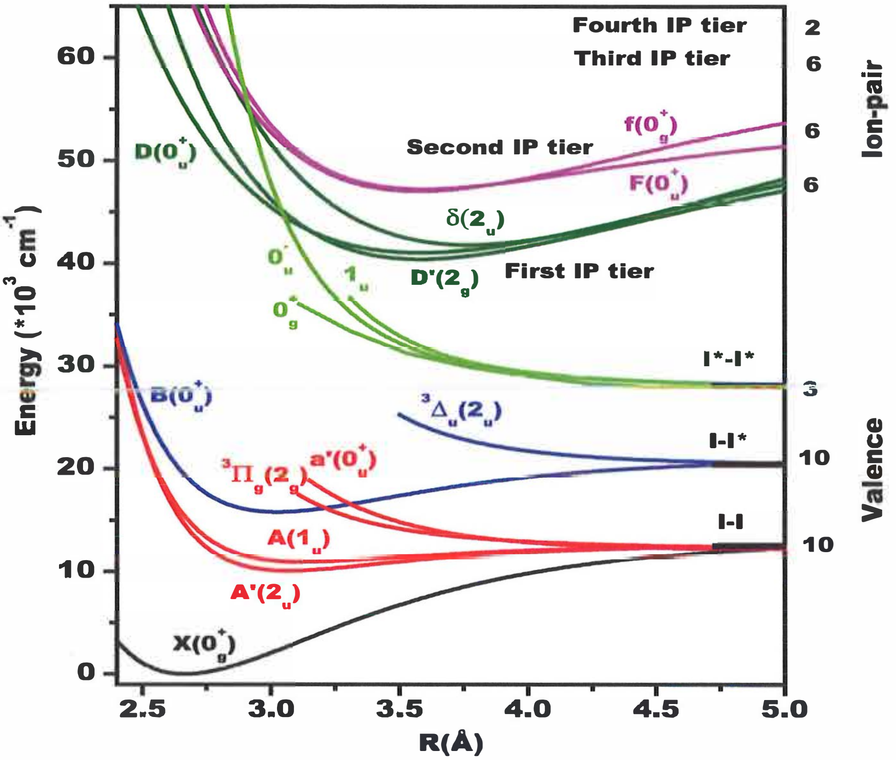

Figure 2-3 Part of the electronic state structure of I_2 in the gas phase. The electronic potentials have been constructed from the data presented in Refs. [31, 33, 39, 41, 49], and the references therein. The shown potentials are color-coded according to their dissociation asymptotes and labeled on the right-hand side of the figure to the "valence" or "ion-pair" manifolds.

2.1.2 Structure, spectroscopy and dynamics of matrix-isolated I_2

Isolation of I_2 inside crystalline rare gases (RGs) has very profound consequences for the spectroscopy of this molecule. The technical aspects of I_2 matrix-isolation are briefly described in Section 4.1, and some of theoretical aspects relevant to matrix-isolation and the spectroscopy of matrix-isolated species are covered in Chapter 3.

Briefly, the heaviest of the rare gases (Ne, Ar, Kr and Xe) form face-centered cubic (fcc) crystalline lattice at low temperatures.[50] These optically transparent van der Waals solids provide excellent media to study photophysical properties of isolated molecules in a relatively weakly perturbing condensed-phase environment. When I_2 is introduced as an impurity to a low-temperature RG crystal, the molecule is considered to dominantly substitute two rare-rare gas atoms in the crystalline lattice.[51-54] Figure 2-4 schematically represents the double substitution environment suggested for I_2 in solid-fcc Xe lattice.[I]

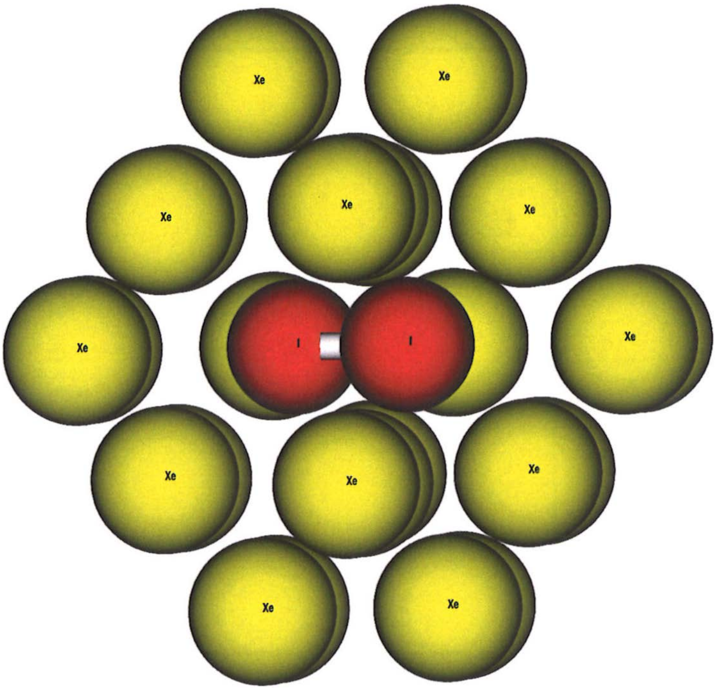

Figure 2-4 Molecular dynamics (MD) simulation of the double substitution site of I_2 in solid Xe at T = 50. Red atoms are the iodine atoms and yellow atoms are the Xe atoms. Figure adapted from publication I. Copyright © 2012 American Chemical Society. By kind courtesy of Toni Kiljunen.

The I_2 molecule itself has effectively only the internal degree of freedom in the RG crystals: the internuclear vibrational coordinate R. This is due to the efficient suppression of all rotational degrees of freedom by the surrounding RG cage.[53,55] Iodine resides dominantly in piston-type vacancies which strictly orient the molecule to coincide with the double-vacancy direction. Iodine inside a low-temperature crystalline RGs thus typically only exhibits purely *vibrational* (or *vibronic*) transitions without any notable rotational fine structure.

The *vibrational* energy levels of isolated I_2 molecules are relatively weakly perturbed by the RG surrounding. For example, small matrix-induced red shifts ($\approx$-1-5 cm^{-1}) of the fundamental vibrational transition energies (G(v=1)-G(v=0)) are typically observed for the ground-state iodine in solid RGs[51,56-61,I] from the gas-phase value of the free molecule (213 cm^{-1}). The absolute magnitudes of the vibrational energy shifts are dependent on the RG host and the electronic state in question, but qualitatively the energies of I_2 vibrational states show larger shifts from the gas-phase values as more polarizable hosts are used for isolation. Unfortunately, the effects induced by the solid RGs to the vibrational energy levels of I_2 are rather poorly known, and the behavior of vibrational energy levels is only known with some accuracy for ground-state I_2. Figure 2-5 illustrates the behavior of the harmonic wavenumber (ω_e) of the ground-state (X) potential in different solid RGs as function of the bulk dielectric constant (ε) of the host.[62]

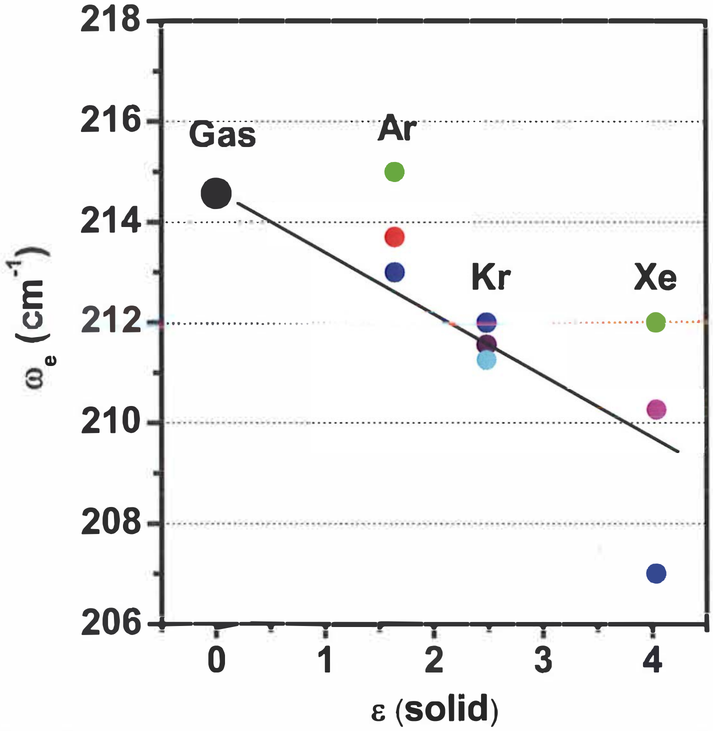

Figure 2-5 Behavior of the ground-state harmonic frequency in different solid RGs. Gas-phase value (•) Ref. [22], green dots (•) Ref. [63], blue dots (•) Ref. [57], red dot (•) Ref. [64], purple dot (•) Ref. [55], cyan dot (•) Ref. [61], and magenta dot (•) from publication I.

The I_2 ground-state spectroscopic parameters have been obtained from various spectroscopic studies of I_2 in solid RGs where the ground-state vibrational energy structure has been studied using relaxed $A(^3\Pi_u(1_u))\rightarrow X$ and $A'(^3\Pi_u(2_u))\rightarrow X$ emissions, Resonance Raman, and time-resolved coherent anti-Stokes (TRCARS) techniques. The reported values show notable discrepancies, but the red-shifting behavior of the ground-state harmonic frequencies can be clearly established when heavier RGs are used to isolate I_2.

The excited *electronic* state energies of iodine are expectedly subject to much stronger energy shifts in solid RGs than the vibrational energy levels. Figure 2-6a shows the matrix shifts of the electronic origins (T_e) for the I_2 valence states A, A′ and B in different RGs. The potential minima of the valence states are typically red-shifted by ~200–600 cm^{-1} from the gas-phase values of the respective states in solid RGs. As with the vibrational level shifts, the red-shifting of the potential minima becomes more prominent with heavier RGs. Solid Xe I_2 typically shows a strong relative increase of the matrix shift compared to other RGs.

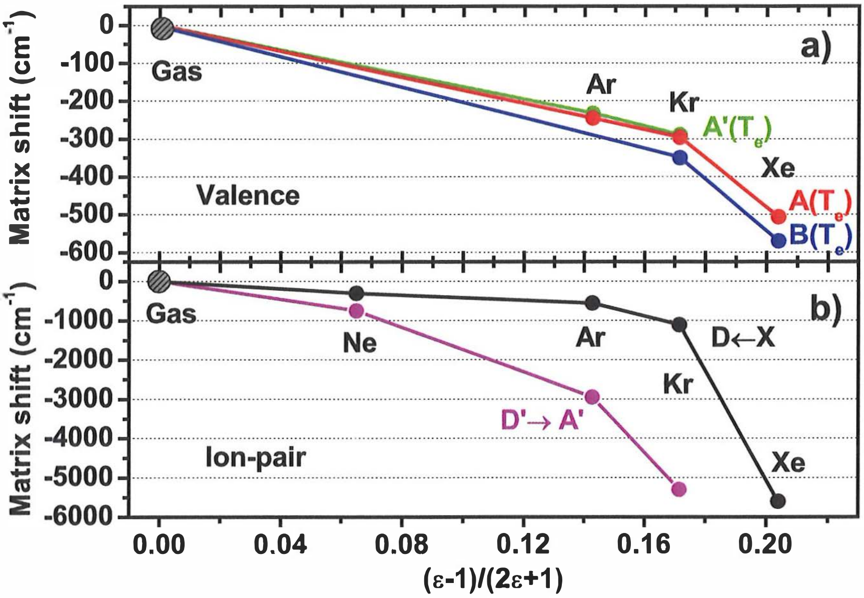

Figure 2-6 a) Matrix shifts of the valence state T_e values in different RGs. Green (•) and red (•) dots in panel a) from Refs. [57, 58] and blue dots (•) from Ref. [65] and publication I; b) Matrix shifts in the transition energies of the IP state absorption (D←X, black dots (•)) and emission (D'→A', magenta dots (•)) in different RGs. Points taken from Ref. [49], apart from the D←X in solid Xe, taken from publication II. The shifts are represented as a function of dielectric constant term $(\varepsilon-1)/(2\varepsilon+1)$ in Onsager's cavity model (see Equation 2-5).

The matrix solvation of I_2 IP states shows rather peculiar behavior in solid RGs as shown in Figure 2-6b. The matrix-effects observed for these states are much stronger than for the valence states. The black dots shows the matrix shift of the absorption maxima of $D(0_u^+)\leftarrow X$ transition in different RGs environments (calculated transition energy in the gas phase is 54700 cm^{-1}, Ref.[49]). In the range from Ne to Kr, the transitions are red-shifted up to ≈ 1000 cm^{-1} from the expected gas-phase value.[49] On the other hand, the relaxed emissions from the first IP tier transitions (shown for $D'(2_g)\rightarrow A'$ with magenta dots in Figure 2-6b) show a shift of over 5000 cm^{-1} in the same range of host materials. This discrepancy has partly been explained by the increase of the equilibrium distances of the IP states ($\Delta R_{e,IP} \approx$ 0.14-0.3 Å)[49,66] in Ar and Kr compared to the gas-phase values. This phenomenon is also debated to occur in the excited valence states of matrix-isolated I_2.[51] However, it has been recently shown theoretically using a DIM formalism that the likely reason for the strong red shifts is the environmentally mediated symmetry breaking of the relaxed IP states in the crystal cavity. The symmetry breaking produces partially charged iodine atoms within the I_2 molecule, which are then strongly red-shifted in energy in the RG environments.[42]

The small matrix shift in absorption, on the other hand, implies that *absorbing* IP states have gas-phase-type symmetry in Ne, Ar, and Kr. Within the classical dipole solvation model introduced by Onsager[67] (and taken as revised by Helbing and Chergui, i.e., the solvation shift ΔE is dependent on R),

$$\Delta E(R) = \frac{1}{4\pi\varepsilon_0}\frac{8(\varepsilon - 1)\vec{\mu}(R)^2}{(2\varepsilon + 1)d^3} \tag{2-5}$$

the weak shift in the absorption can be taken as indication that no significant dipole ($\vec{\mu}(R)$) is present when the IP states are probed in the ground-state configuration (R = 2.666 Å). Interestingly, our recent results suggest that this not the case in solid Xe where the absorbing D-state is strongly polar (see Figure 2-6b, Xe).[II] Note that the IP states emissions of I_2 cannot be directly observed in solid Xe. The IP states predissociate to the valence states upon excitation.[II]

Iodine in solid RGs is a many-body system, and in this sense, even though the system is at first glance simplified by the lack of rotational degree of freedom, the complication of the system arises from the strong coupling to the RG environment. The energy shifts in the vibrational and electronic energy levels are of course a manifestation of the interaction of the molecule with its environment. More direct implication of the many-body nature of the system can be seen in the electronic state potentials of I_2 in solid RGs. Figure 2-7 shows the shapes of the X- and B-state potentials in a crystalline fcc Xe lattice. Near the equilibrium distances of the gas-phase potentials ($R_e(X)$ = 2.666 Å and $R_e(B)$ = 3.045 Å),[22] these potentials resemble the gas-phase potentials, and it has been shown on many occasions that the gas-phase type Morse-potentials

$$U(R) = D_e[1 - \exp(-\alpha(R - R_c))]^2 \tag{2-6}$$

with vibrational energy term values (with power expansion beyond the Morse description)

$$G(v) = \omega_e\left(v + \frac{1}{2}\right) - \omega_e x_e\left(v + \frac{1}{2}\right)^2\left(+\omega_e y_e(v + \frac{1}{2})^3 - \cdots\right) \tag{2-7}$$

can give a reasonably accurate description of the I_2 valence potentials near the vicinity of the potential minima (see for example, Ref. [61]). However, at elongated bond distances (in Figure 2-7, R > 4 Å) the potential energies show a steep rise, and the simple Morse description fails. This is the "cage effect" of the surrounding RG atoms,[68] which prominently affect the spectroscopy of I_2 in solid RGs. For example, the dissociative I*-I* potentials are strongly stabilized in the RG cages, in a way that fluorescence from the repulsive states is readily observable.[69] The RG atoms at both ends of the I_2 molecule (see Figure 2-4) suppress the permanent molecular dissociation when the system is photoexcited over its dissociation limit. In the event of apparent molecular dissociation (excitation over the dissociation limit), the molecular fragments are forced to recombine by the surrounding cage atoms. Photodissociation of the I_2 molecules in solid RGs thus typically have a probabilistic nature, depending for example on the excess energy deposited in the system.[70]

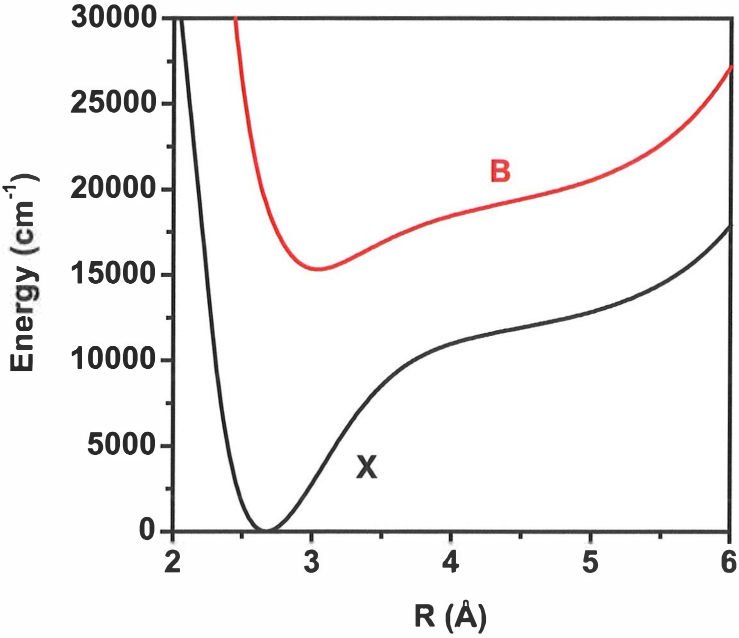

Figure 2-7 X and B state potentials in solid Xe. Potentials obtained from molecular dynamics (MD) simulation of I_2 in a double-substitutional cavity in fcc Xe lattice at T = 50 K. Figure adapted from publication I. Copyright © 2012 American Chemical Society. By kind courtesy of Toni Kiljunen.

Electronic absorptions and emissions of I_2 in RG solids are typically characterized by broad Franck-Condon (F-C) envelopes with no distinctive rovibronic fine structure (for B←X absorption, see for example Refs. [64], [71]). This is in clear variance with the gas-phase I_2, where rich densities of rovibronic transitions for numerous electronic transitions can be easily observed (for example, Ref. [29]). In solid RGs the only known exceptions to this case are the long-lived A→X and A′→X transitions, which show broad vibronic structures in the relaxed emission.[51,57,63] The lack of vibronic fine structure for I_2 in solid RG has been attributed to the extremely fast *electronic dephasing* in the excited states.[72,73] For the I_2 B-state the time scale for electronic dephasing has been established to occur during the first extension of the excited state molecule (~ 100 fs).[74,75]

Iodine isolated in solid rare gases (I_2/RG) is in many ways a very prototypical model system for solid-phase many-body photodynamics.[76] The system has been a subject of numerous femtosecond (fs) pump-probe studies in solid RGs.[52,53,66,68,70,71] Most of these ultrafast studies have utilized pump-probe schemes where the low-energy valence states (usually A or B) are initially excited by an optical fs-pulse (pump). The ensuing coherent dynamics of the vibrational wavepacket on an excited valence state is then probed using another delayed fs-pulse (probe) through the laser induced fluorescence (LIF) from the IP states. A typical result of such a two-color pump-probe experiment is shown in Figure 2-8. The central interest in these studies has been the many-body nature of the I_2 dynamics in solid RGs, namely the caging and the recombination event of the molecule,[52,68,70,77] the dynamics of environmentally mediated vibrational relaxation, and the predissociation to the other valence states[65,66,71]. Much of this earlier pump-probe work has been reviewed by Gühr *et al.*[73] and also by M. Gühr in his PhD dissertation.[78] The above studies have shed light to the relevant time scales for the different dynamical processes occurring in the I_2 molecule trapped in the RG cage.

The ground-state potential of I_2 in solid RGs and the vibrational decoherence induced by the pure dephasing in this state have also been subject of a series of TRCARS studies by Apkarian and colleagues.[60,61,79] The extremely long-lived vibrational coherences (typically from tens to hundreds of picoseconds depending on the v-state and the temperature) can by probed using the TRCARS technique, where the evolution of vibrational wavepackets on the ground state are interrogated using a third fs-pulse, generating a third-order nonlinear polarization $P^{(3)}$ emitting a CARS photon. The studies of I_2/RG systems using these time-dependent four-wave mixing techniques (FWM) have suggested that the dominant dephasing mechanism for the ground-state molecule is *pure dephasing* through the pseudolocal phonon modes. More recently, the dynamical studies of solid I_2/RG systems have focused on the generation of vibrational/electronic coherences on the B-state and interrogating the quantum nature of the transients using similar four-wave or six-wave mixing techniques.[72,74,75]

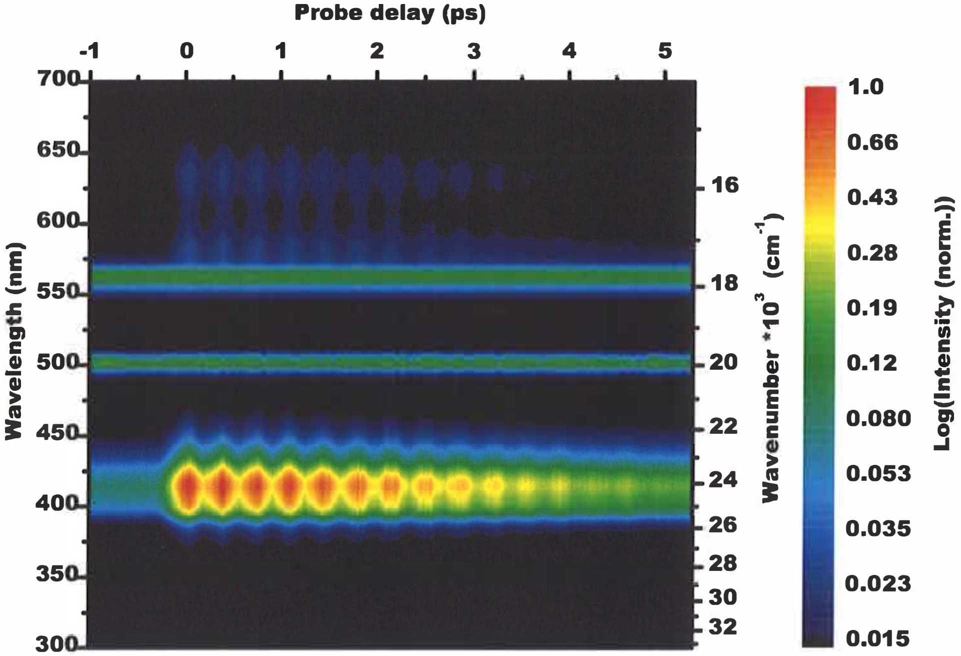

Figure 2-8 Pump-probe measurement of I_2/Xe/Kr = 1/2.6/2600 at T = 40 K using λ_{PUMP} = 558 nm and λ_{Probe} = 500 nm. Despite the presence of Xe in the sample, the shown dynamics reflect the vibrational dynamics of B-state I_2 in solid Kr. From publication II. Copyright © 2012 American Institute of Physics.

2.2 Complexes of iodine

2.2.1 I_2-Xe

A vast number of experimental and theoretical studies can be found in the literature regarding structure, dynamics and energetics of halogen-RG complex systems in the gas-phase RG clusters (see for example, Refs. [80-83]). This field has been recently reviewed by Beswick *et al.*[84] Despite the great efforts to understand tri-atomic van der Waals complexes, few gas-phase studies actually concern directly the I_2-Xe complex. The structures of the ground-state complexes have been under great debate in the literature on clusters. The current consensus regarding the structure of the RG-I_2 complexes is that there are two dominant isomers: T-shaped and linear complexes that can co-exist in gas-phase environments.[84] Similarly, the DIM calculations related to the condensed-phase I_2-Xe complexes have shown that the two isomers are very close in energy,[39,85] and often there is no clear spectroscopic distinction between the two structures. According to recent *ab initio* calculations of the I_2-Xe complex, the difference in the stability of these two isomers is approximately 58 cm^{-1} in favor of the linear complex.[86]

Much effort has also been invested in studying the relaxation of I_2 in gas-phase bulk Xe. Recent double-resonance excitation works by Pravilov and colleagues have given some indication of I_2-Xe complex presence in the samples containing I_2 in the bulk Xe gas.[87,88] The complexes have been presumably detected in emission upon excitation of the I_2 IP states. Potter *et al.* have also proposed bimolecular reaction control of I_2-Xe complex dissociation through a harpooning mechanism, using a femtosecond pump-probe excitation through the gas-phase I_2 B-state in the presence of Xe.[89]

It has become evident from the works by Pravilov and colleagues that the I_2-Xe complex is a rather elusive species in electronic spectroscopy. Therefore, very little is actually known about the electronic state structure of the iodine-xenon 1:1 complex. This situation concerns condensed-phase environments in particular, as only very few studies of this complex exist. In this regard, the matrix isolation studies of the I_2-Xe complex in solid Kr by Kiviniemi *et al.* are very valuable, because they have enabled the study of purely *isolated complexes* with well defined structures.[85] Near perfect isolation of the van der Waals complex dimer inside a crystalline Kr lattice can be obtained by choosing suitable matrix-preparation parameters (I_2/Xe/Kr -ratio, matrix deposition temperature and matrix deposition rate, see 4.1). The presence of the ground-state complex can be verified using high-resolution resonance Raman or TRCARS techniques.[85,A3]

Figure 2-9 shows a typical TRCARS trace where the presence of the I_2-Xe complex can be identified in the *polarization* beating between the uncomplexed I_2 and the I_2 molecule in the Xe complex.[85,A3] The studies by Kiviniemi *et al.*[85] have shown that the I_2 molecule in a Xe complex has a weakly altered ground-state potential compared to the "free" I_2 molecule isolated in solid Kr ($\Delta\omega_e$ = -0.90 cm^{-1}, $\Delta\omega_e x_e \sim 0$). The vibrational dephasing times in the solid-phase complex are only weakly decreased compared to the I_2 molecule in solid Kr. These studies have also given order of magnitude estimation of the complex abundance, suggesting that the amount of the complex in solid Kr is highly unstatistical in comparison to the total amount of Xe in the samples. The MD calculations using DIM potentials for the complex have also given estimation for the ground-state binding energy ($\approx$ 285 cm^{-1}) for the linear complex, tentatively assigned as the most stable complex structure in solid Kr.[85] Recent *ab initio* calculations for the gas-phase I_2-Xe complex have also resulted in the same conclusion about the minimum energy structure; moreover, the calculations indicate very similar binding energies for the linear structure.[86]

The interesting question about the isolated I_2-Xe is complex is whether it can be observed in electronic spectroscopy. In other words, is there a distinctive signature for the complex in the excited states that identifies the species, similarly to the ground-state complex as shown in Figure 2-9. This question is addressed in Section 5-2 and in publication II.

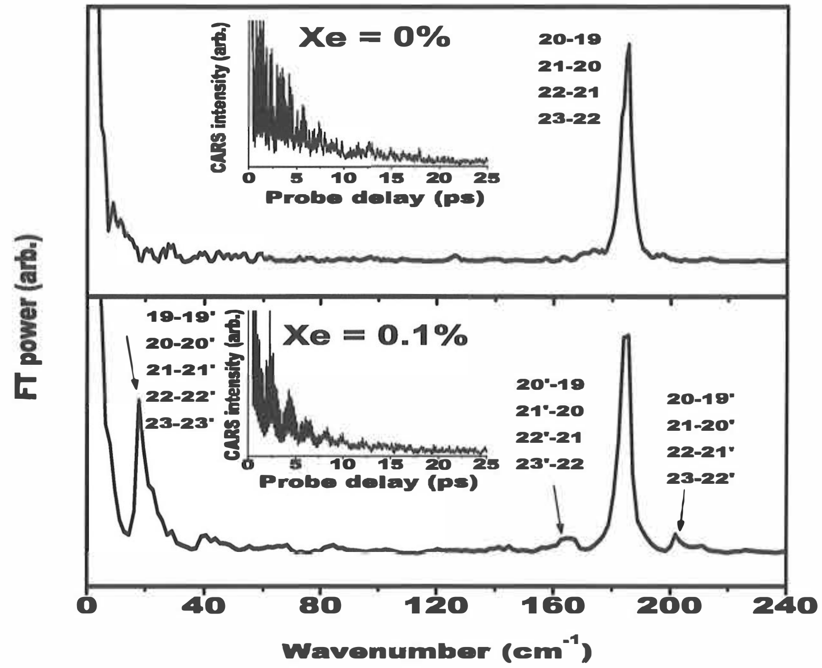

Figure 2-9 Energy-domain TRCARS spectra (main panels) and the corresponding time-traces (insets) of I_2/Kr = 1/2600 and I_2/Xe/Kr = 1/2.6/2600 at T = 10 K. The lower spectrum shows the signature of the I_2-Xe complex in the additional polarization beat frequencies (marked by arrows) of the high-energy ground electronic state wavepacket ($v'' \approx 20$). From publication II. Copyright © 2012 American Institute of Physics.

2.2.2 $(I_2)_n$

Small neutral aggregates and aggregate-type species of molecular iodine ($(I_2)_n$) are known to exist in all possible phases. For example, presence of neutral dimers of $(I_2)_2$ have been reported in the vapor phase by Tamres *et al.*[90] The formation enthalpy ~12 kJ/mol at T = 605 K for the gas-phase dimer has been deduced from the spectroscopic data by Passchier and Gregory.[91] Very similar evidence of the presence of $(I_2)_2$ has also been obtained in the earlier UV-region spectroscopic studies of I_2 in liquid CCl_4 and n-heptane.[92,93] The photodissociation studies of iodine by Philippoz *et al.* in the gas-phase clusters ($(I_2)_a$-$(M)_b$, where M = RG, H_2, N_2, O_2 or I_2) clearly indicate I_2 aggregation, mainly attributed as a formation of I_2 dimer ($(I_2)_2$) in low-temperature clusters.[81,94]

More recently, aggregates of I_2 have been investigated by several groups in nanoporous TiO_2[14,95]. The optical activity of the TiO_2 particles can be increased by introducing $(I_2)_n$ aggregates in the nanoscopic pores of the material. The properties of I_2 aggregates have also been studied in nanoscopic zeolite crystals.[96,97] Wire-like molecular aggregates of I_2 inside the zeolite channels are proposed as the source for the distinctive Raman transitions in these studies.

In the liquid phase, the X-ray diffraction studies of molten $I_2(l)$ by van der Marel *et al.*[98] also suggest that the remnants of the I_2 crystalline structure may be partially preserved through short-range interactions even in the high-temperature liquid phase, evidencing a liquid-phase I_2 aggregate species. Raman studies of liquid iodine by Magana and Lannin have yielded similar results, suggesting the presence of long-lived $(I_2)_n$ liquid-phase clusters.[45,46]

Neutral matrix-isolated I_2 aggregates have also been observed in low-temperature crystalline Ar in UV-absorption and in laser photoluminescence by Andrews and colleagues.[99,100] Raman spectroscopy of matrix-isolated I_2 has proven a very informative tool in this regard to study the I_2 aggregates. Clear signatures of such species have been obtained in different RGs in the seminal Raman works by Andrews,[64] which have since been reproduced by other authors.[101,III] In solid RGs, the I_2 aggregates were previously assigned to correspond with the fundamental Raman transition at $\omega = 180\ \mathrm{cm^{-1}}$, which is nearly identical to the in-phase transition observed in bulk crystalline iodine (see section 2.1.1). This bulk-like 180 $\mathrm{cm^{-1}}$ transition in the low-resolution Raman studies of solid RGs has been assigned to clusters with possibly 2-4 iodine molecules ($(I_2)_{2\text{-}4}$).[64] This assignment is defined in greater detail in publication III.

The evidence of existence of $(I_2)_n$ species is rather overwhelming, as shown by the numerous studies above. The existence of $(I_2)_n$ complexes is not very surprising at all if one considers that the iodine is a well-organized molecular solid in room-temperature ambient conditions. However, in reality very little is known about the structures and properties of I_2 aggregates. This raises an interesting question: What kind of intermediates there are between crystalline I_2 and gas-phase I_2, and what is the limit of molecules in the cluster when the "bulk" phase is reached? This question is addressed in section 5.3 and in the original publication III.

2.3 $\mathrm{Au_{102}(p\text{-}MBA)_{44}}$

The extensive study of monolayer-protected nanoscopic gold clusters begun when Brust *et al.* published their work on a simple organothiolate-based synthesis scheme for producing gold nanoparticles in the size range of 1-3 nm.[102] The qualitative two-stage reaction scheme is shown by the following equations (adapted from Refs. [103] and [104]):

$$[\mathrm{Au^{III}Cl_4}]^{-1} + \mathrm{RSH} \rightarrow (-\mathrm{Au^{I}SR}-)_\mathrm{q} \tag{2-8}$$

$$(-\mathrm{Au^{I}SR}-)_\mathrm{q} + \mathrm{BH_4^-} \rightarrow \mathrm{Au_x^0(SR)_y} \tag{2-9}$$

In the first stage of the reaction, the gold and the organothiolate precursors (RSH) produce Au-thiolate polymer, which is then reduced (typically using

$NaBH_4$) to yield gold clusters of various sizes. Variations of this "Brust-Schiffrin synthesis" and other synthetic techniques have been developed to produce monolayer-protected gold nanoparticles with different types of ligands[104] (see, for example, the water-soluble variants in Ref. [105]). The problem with the cluster synthesis is that the above equations typically yield products of various different sizes (x and y, in Equation 2-9) depending on the preparation parameters.[103] Thus the separation of different-sized clusters from each other has been, and still is, the real challenge in the studies of atomically precise Au clusters. Many experimental techniques, such as polyacrylamide gel electrophoresis (PAGE), are nowadays available to separate different sizes of clusters from one another. Some of these techniques were recently reviewed by Tsukuda[104] and will not be repeated here.

A real breakthrough in the research of atomically precise thiolate-protected gold nanoclusters was obtained when Jadzinsky *et al.* reported the total structure determination of the stable Au_{102}(p-MBA)$_{44}$ cluster with 1.1 Å precision.[106] Reproduction of the X-ray crystal structure of the cluster is shown in Figure 2-10A. The X-ray study by Jadzinsky *et al.* showed that a gold nanocluster with an approximate Au mass of ~21 kDa consists of precisely 102 Au atoms surrounded by 44 para-mercaptobenzoic acid ligands ($-SC_6H_4COOH \equiv -SR$, see Figure 2-11A) covering the surface of the water-soluble particle. A later theoretical study by Walter *et al.*[107] found that the structure of the cluster can be understood of consisting of a "metallic" core with 79 Au atoms and a "protective" thiolate-gold layer consisting of Au_{23}-SR_{44} (See Figure 2-10B, C and D). The core of the cluster has a high degree of 5-fold D_{5h} symmetry, which is only slightly perturbed by the irregular positions of the 13 Au atoms at equatorial positions perpendicular to the ~D_5 symmetry axis (see Panel B, where the core is depicted from the top along the symmetry axis).

One of the most intriguing findings in the X-ray crystal structure of Au_{102}(p-MBA)$_{44}$ are the peculiar "staple"-bonding motifs of p-MBAs and the gold atoms. These ring-like Au-SR units clearly vary from the so-called standard model, where a direct connection of the single p-MBA ligands to the core is expected.[108] These staple structures are shown on the surface of the Au core by yellow-orange (gold-sulfur) sticks in C and D panels of Figure 2-10 and represented schematically in Figure 2-11B and C. The staple motifs consist of p-MBA ligands (-SR) connected via sulfur to the surface of the gold core ((Au)). The ligands are bridged by a gold atom between the p-MBAs. These staple-like ring structures follow the predicted "divide-and-protect" concept introduced for smaller thiolate- or phosphine-protected Au clusters by Häkkinen *et al.*[109] The Au_{102} structure contains two types of staple structures, as shown in Figure 2-11: single staples (-SR-Au-SR-) and double staples ($-SR-(Au-SR)_2-$). There are altogether 19 single units and 2 long double stable units connected to the surface of the Au core. The gold atoms in the core of the cluster are essentially metallic (Au^0), but the gold atoms in the $-SR-(Au-SR)_x-$ units ($x = 1$ or 2) are in an oxidized-state (Au^I):

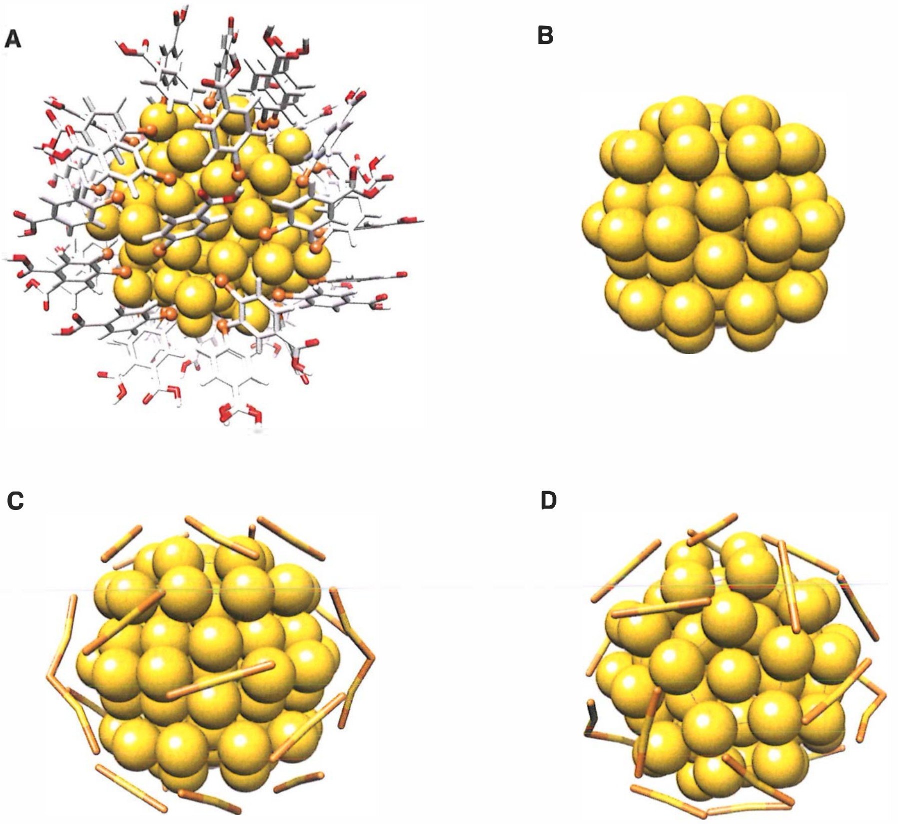

Figure 2-10 Reproduction of the $Au_{102}(p\text{-MBA})_{44}$ crystal structure A) the full cluster B) Au core C) and D) with the staple motifs included as sticks. Figure from publication IV. Copyright © 2011 American Chemical Society.

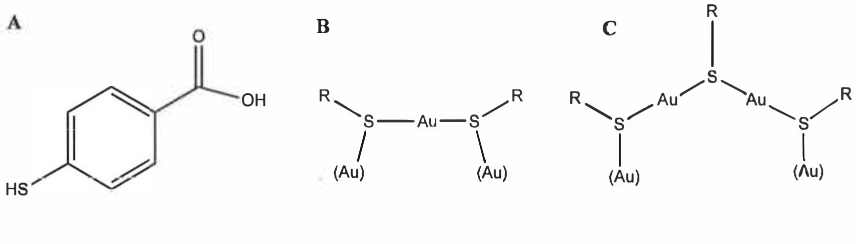

p-MBA (H-S-R) "Staple" motif "Double staple" motif

Figure 2-11 Schematic illustration of single p-MBA structure and the staple motifs covering the $Au_{102}(p\text{-MBA})_{44}$ cluster A) single p-MBA thiol B) single staple C) double staple. Staple motifs reproduced from Ref. [110]

The $Au_{102}(SR)_{44}$ cluster has been the subject of many theoretical calculations and debate about the stability of the cluster, ever since the structure was obtained.[107, 111-114] Theoretical LR-DFT studies by Häkkinen and colleagues have shown that the "magical" stability of this cluster can be traced back to several factors: Existence of a major HOMO-LUMO gap (predicted energy ~0.5 eV) due to an electron shell closure of a delocalized superatom orbital, with a G-type character, chemical steric passivation of the gold surface by the protecting gold-ligand layer, and the formation of a symmetrical core that can sustain the electronic shell structure.[107,115]

The electronic shell closure in Au_{102}(p-MBA)$_{44}$ has been attributed to a so-called "58 electron" shell closure, which shows exceptional stability, in bare gold clusters.[116] This electron closure number in the cluster can be understood as localization of the 21 "excess" Au($6s^1$) electrons of the Au core (in total 79 Au atoms) to the bond formation with the 21 thiolate units, resulting in nominal shell closure of the core Au atoms and increased electronic stability of the cluster. The calculated electron density of states (angular-momentum-projected local electron density, PLDOS) for the model cluster $Au_{102}(SMe)_{44}$, where Me stands for methyl ($-CH_3$), is shown in Figure 2-12. Previous works by Walter *et al.* have shown that the calculated electron densities for the model clusters with SMe-ligand or p-MBA-ligand are virtually identical.[107] The calculated electron density shows a clear ≈ 0.5 eV gap between the HOMO orbitals with dominantly superatomic "G" character (section c, ≈ -0.5-0 eV, three top panels Figure 2-12) and the LUMO orbitals (section d ≈ 0.5-0.75 eV, Figure 2-12) with a superatomic 'H' character.

It is perhaps noteworthy that the superatomic description of atomically-precise $Au_x(SR)_y$ clusters proposed by Häkkinen and colleagues[107] has been very successful in predicting exceptional stability of other gold nanoparticles. For example, the total-structure determined cluster $[Au_{25}(SPhC2)_{18}]^-$ [117,118] is a species that exhibits "8 electron" shell closure, which is another stable number of bare s^1 open shell clusters.[116] The simple stability-counting equation for the monolayer protected Au clusters takes the form:[107]

$$m^* = N\upsilon_A - L - q \tag{2-12}$$

where m^* is the magic shell-closing number in bare clusters (m^* = 2, 8, 18, 34, 58, 92, etc.), N is the number of core Au atoms (with atomic valence $\upsilon_A = 1\ (6s^1)$), L is the number of electron withdrawing ligands and q is the total charge of the cluster. Interestingly, it has recently been suggested that electronic shell closures contribute even to the stability of large "plasmonic" $Au_{333}(SR)_{79}$ clusters with no apparent HOMO-LUMO gap.[119] However, it has been predicted that in larger cluster other forces may play a role in defining the stability of the cluster, such as the formation of highly symmetrical core structure as predicted for $Au_{144}(SR)_{60}$.[120]

From a purely experimental spectroscopic point of view, the ability to produce pure Au_{102}(p-MBA)$_{44}$ in reasonably large quantities is necessary condition for accurate measurements of the electronic structure of this cluster. Levi-Kalisman *et al.* recently published a scheme to produce Au_{102}(p-MBA)$_{44}$ on a preparative scale that yielded essentially pure cluster (see also section 4.2).[121]

This synthetic and preparative work enabled the spectroscopic studies in publication IV.

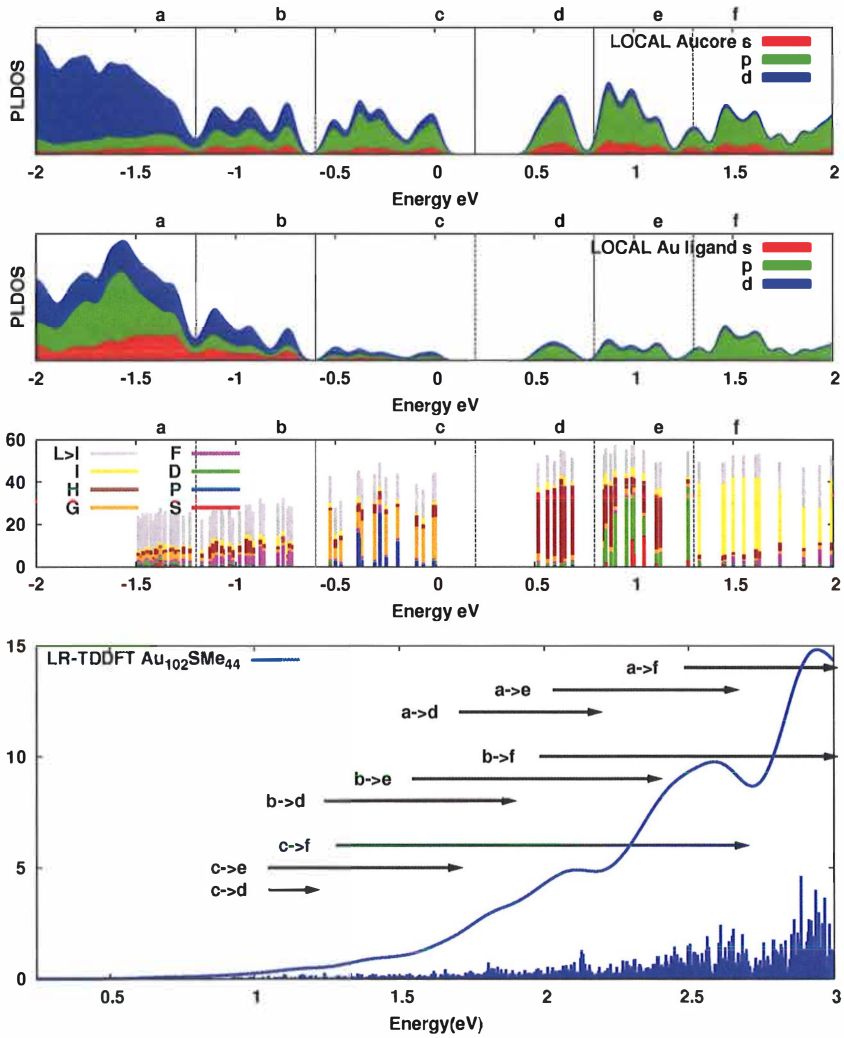

Figure 2-12 The top three panels show the decomposition and weight of different types of orbitals in the angular-momentum projected local electronic density of states (PLDOS) for the $Au_{102}(SMe)_{44}$ model cluster calculated at the LR-DFT level of theory. The local DOS has been decomposed to fully occupied orbitals (regions **a,b,c**) and unoccupied orbitals (regions **d,e,f**), with the weight of the localization of the Kohn-Sham orbitals to the Au_{79} core (top), the ligands (second from top), and the corresponding super-atomic character (third from top). For more information see supporting information in publication IV and Ref. [107]. The lowest panel shows the calculated optical transitions for the model cluster (blue sticks and the convoluted blue spectrum). The spectrum shows also qualitative identification of the transitions from different regions of the local DOS. From publication IV. Copyright © 2011 American Chemical Society.

3 SOME CONCEPTS OF CONDENSED-PHASE SPECTROSCOPY

In order to clarify the discussion in Chapter 5, some concepts relevant to condensed-phase spectroscopy need to be established. Publication I reports sharp vibronic structures in the B↔X transitions of I_2 in solid low-temperature Xe, which implies long-lived electronic coherence in iodine and the existence of zero-phonon lines (ZPLs). Thus these concepts should be defined. Actually the discussion about coherences is relevant to all the spectroscopic results presented in this thesis. For example, the absorption spectrum of Au_{102}(p-MBA)$_{44}$ in publication IV (discussed in more detail in the upcoming chapters) is nearly structureless, with no apparent vibronic structures. This naturally evidences extremely fast electronic dephasing in the room-temperature cluster upon excitation. Even though the few concepts highlighted in this chapter are most relevant to publication I, they often underlie the spectroscopic results in other publications.

3.1 Coherence and dephasing

Condensed-phase molecular systems are far from being isolated. The interaction of the system with the surrounding matter (often called the *bath*) induces the system population to relax and the coherences to dephase. The concept of "coherence" is central to condensed-phase spectroscopic studies, but possibly even more important is the concept of "dephasing": this is because the dephasing (i.e. loss of phase correlation between quantum states), or more accurately the dephasing time, defines the *linewidth* of a transition. For example, the (normalized) absorption spectrum in the absence of inhomogeneous line broadening mechanisms is given by [122]

$$\sigma(\omega) = \frac{1}{\pi} \frac{\Gamma}{(\omega - \omega_{01})^2 + \Gamma^2} \tag{3-1}$$

The above equation is for a system with only two distinct states, which are coupled by a light field with a frequency of ω_{01}. The energy spectrum of a transition is a Lorentzian function with a width Γ. The width of a naturally broadened (i.e., homogenous) line (in units of cm^{-1}) is given by[123]

$$\Gamma[\mathrm{cm}^{-1}] = \frac{1}{c\pi T_2} \tag{3-2}$$

where $1/T_2$ is the total dephasing rate of a transition. The dephasing rate consists of two contributions[123]

$$\frac{1}{T_2} = \frac{1}{2T_1} + \frac{1}{T_2^*} \tag{3-3}$$

namely the *dissipation* T_1, and the *pure dephasing* T_2^*. In crystal environments the pure dephasing contribution to the total dephasing arises from the elastic scattering of phonons and the chromophore, and is often the dominant mechanism of the dephasing. The dissipation contribution arises from population relaxation of the excited state, typically occurring via non-elastic collisions with the phonons. When absorption linewidths and dephasing are described phenomenologically in the condensed phase, a rather intuitive picture of the phenomenon is given by Heller's time-domain description using quantum autocorrelation functions:[124]

$$C(t) = \langle \Psi(0) | \Psi(t) \rangle \tag{3-4}$$

Where the correlation function $C(t)$ is the overlap between the initial wavepacket (= initial wavefunction multiplied by transition dipole moment to the excited state) and the evolving (time-dependent) wavepacket on the excited state. The absorption spectrum in this case is given by Fourier transform of correlation function

$$\epsilon(\omega) = B\omega \int_{-\infty}^{\infty} C(t)\, e^{-i(E+\omega)t}\, dt \tag{3-5}$$

where ω is the frequency of the incident radiation, E is the energy of the initial wavefunction, and B is a constant term. A necessary condition for vibronic structure in the electronic absorption spectrum is the *recurrence* of the overlap in

C(t).[124] The absorption spectrum and the correlation function are Fourier transform pairs, where the overall decay of the *C(t)* gives the linewidth of the vibronic transitions.[125] The Fourier transform of the absorption spectrum to the time-domain is naturally the correlation function. In the condensed phase this Fourier transform of the absorption spectrum can be understood as giving the full many-body correlation function, including the environment response.[126] In the time-domain the overall decay of the *C(t)* as function of the time is inversely proportional to the full dephasing time T_2, and thus to the linewidth of a vibronic line.

The concept of "coherence" is usually described using the density operator formalism (see, for example Refs. [78],[122]). The *coherences* in this description are the off-diagonal elements of the density operator, and the *populations* of the states are the diagonal elements. Equation 3-6 shows the time evolution of a density operator describing a coherent superposition of two states in the presence of phenomenological dephasing. The situation describes a decay of a superposition state $\Psi = a|0\rangle e^{-i\omega_0 t} + ib|1\rangle e^{-i\omega_1 t}$, generated, for example, by a light field that has already passed the system (Example taken from Ref. [127]). The system coherences in this case decay with a time constant T_2 and the excited population relaxes to the ground state with a time constant T_1.

$$\rho(t) = \begin{pmatrix} 1-|b|^2 & iabe^{-i\omega_{01}t}e^{-t/T_2} \\ -iabe^{+i\omega_{01}t}e^{-t/T_2} & |b|^2 e^{-t/T_1} \end{pmatrix} \tag{3-6}$$

In a qualitative sense, the "coherence" can be understood as a sustained phase relation between two states of the system and the "dephasing" as the irreversible decay of the phase correlation (often also called *decoherence*). Such phase relations between the states of the system will be generated by an interaction of the system and the electromagnetic fields. There are effectively two types of coherences which are relevant to this thesis: vibrational and electronic. When a resonant light field generates coherences between two states belonging to two different electronic states of a molecule, the coherence is called *electronic coherence*. The optical absorption spectroscopy usually probes this coherence through the field generated by the first-order macroscopic polarization $P^{(1)}$.[122] If, on the other hand, the states with phase relation belong to the same electronic state, the system is said to be in the *vibrational* coherence. For example, pump-probe spectroscopy typically probes the coherence between vibrational states belonging to the same excited state. The important thing about electronic absorption spectroscopy is that the technique does *not* distinguish between the different dephasing mechanisms in Equation 3-3; it merely measures the total dephasing rate $1/T_2$ of the electronic transition (pure dephasing and/or population relaxation due to various reasons).[128]

3.2 Phonon coupling

As stated in the previous section, molecules in the condensed phase are not isolated from their environment. Molecules in crystalline hosts are subject to the phonon bath of the crystal environment. This is one of the physical origins of dephasing in crystalline lattices.[123] The phonon coupling gives rise to another phenomena often observed in low-temperature crystalline lattices. This is the splitting of electronic or vibrational transitions to zero-phonon lines (ZPL) and phonon-side bands (PSB). Figure 3-1 shows a spin-orbit transition of atomic iodine in solid Xe.

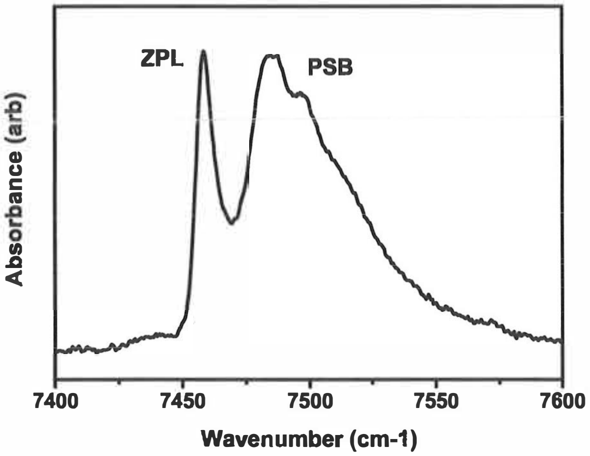

Figure 3-1 Spin-orbit transition $^2P_{1/2}\leftarrow{}^2P_{3/2}$ of atomic iodine in solid Xe at T = 7 K. Adapted from Ref. [129]

The absorption line of atomic I in low-temperature solid Xe in the NIR region is composed of two types of transitions: a sharp ZPL and a broader PSB. These types of ZPL + PSB transitions are reasonably common for very low-temperature crystal-chromophore systems.[130-133] The ZPL can be understood as purely molecular (or atomic) transition between two states of chromophore, without a change of the phonon n state in the surrounding crystal. In electronic absorption this means that the vibronic transition $v''= a \rightarrow v'= b$ is accompanied with a phonon transition $n''= i \rightarrow n'= i$ ($\Delta n = 0$). The PSB, on the other hand, is a molecular transition and a simultaneous change in the phonon state of the crystal environment. In electronic absorption of a system in the ground phonon state this means phonon transition $n''=0\rightarrow n'=1$ (and possibly $n''=0\rightarrow n'=2$ and higher phonon transitions $n' > 2$). The energy difference of the ZPL and the PSB transitions (containing typically several unresolvable modes) correspond to the energy needed to create a (single or multiple) phonon in the vicinity of the chromophore. In many cases, the shape of the phonon band is well described by the single phonon density of states of the corresponding solid.[128] However, the presence of impurities in a crystal generates additional phonon modes, known as the local modes, which will also contribute to the PSB.[134] The ZPLs and PSBs in electronic absorption and emission originate from the displacement of the ground- and excited-state potentials in the configuration coordinate Q, which describes the other degrees of freedom of the surrounding lattice.[126,78].

The magnitudes of the phonon coupling strengths of vibronic (or vibrational) transitions are usually described with dimensionless Huang-Rhys coupling constants:[128,131]

$$S - \ln\left(\sum_{n=0}^{\infty} \frac{I_n}{I_0}\right) \tag{3-7}$$

where the logarithmic ratio in the sum compares the intensity of the whole vibronic structure to the intensity of respective ZPL. I_0 in Equation 3-7 is the intensity of the ZPL. The intensity is usually well described by the area of the transition.[I] The sum term ($\sum I_n$) is the intensity of the whole vibronic transition (~combined area of ZPL and PSB).

4 METHODOLOGY

4.1 Matrix isolation of I_2 and its complexes

Solid RG samples containing iodine and iodine-complexes were prepared using a *matrix-isolation* technique. Matrix-isolation of molecules, atoms and transient species inside solid RGs is a well-established technique, originating from pioneering work by Pimentel and colleagues in the mid-1950s.[135] Many excellent reviews on the subject can be found in the literature.[73,76,131,136,137] For a more comprehensive review of matrix sample preparation techniques and instrumentation the reader is directed to the book on the subject by Dunkin.[138]

The crystalline I_2/RG (where RG = Kr, Kr + Xe or Xe) matrix samples were prepared by the slow continuous-deposition method. In this method, a gas mixture of I_2 and RG was initially prepared at room temperature in high-vacuum conditions in to a 5 dm^3 glass bulb (typically evacuated to base pressure of $p \approx 10^{-6}$ mbar). The gas mixture was prepared by letting a purified solid I_2 (located in another bulb) expand in the sample-preparation vacuum system. When the iodine reached a stable vapor pressure in the vacuum system (typically 0.20-0.30 Torr), the solid I_2 sample was sealed off from the system, and the RG host was added until a pressure ratio of $p(I_2)/p(RG) \approx 1/2600$ was reached. We used commercial Kr and Xe RGs (Aga) without additional purification. In the case of mixed gas mixtures (I_2/Xe/Kr), the ratio of $p(Xe)/p(Kr)$ was varied between 0.001-1, but the total ratio $p(I_2)/(p(Kr)+p(Xe)$ was usually kept constant at 1/2600.

The crystalline sample was prepared by slowly spraying, i.e. *depositing*, the premixed I_2/RG (typically at 0.07-0.13 mmol/min) on a cooled sapphire substrate (thickness ~100-150 μm) mounted inside a vacuum-pumped cryostat (Janis Research Company, He flow cryostat or ADP Cryogenics, closed-cycle He cryostat) equipped with quartz or MgF_2 windows. Different temperatures of the substrate (i.e. deposition temperatures) were used in the range T = 10 – 50 K during the deposition of the sample. The temperature of the substrate was controlled during the sample preparation and the optical measurements using a

Lakeshore temperature controller. Typically a total deposition amount ~2 - 6 mmol of the total gas-phase sample was used to prepare the crystal sample. Deposition was usually stopped when the violet color of I_2 was visually detected in the crystalline sample.

Optically high-quality I_2/Kr samples, with purely isolated I_2 molecules, i.e. *monomeric* I_2 matrices, can be obtained using a deposition temperature of T = 40 K. This result can be verified using Raman or TRCARS techniques.[III] The monomericity of I_2/Kr samples using lower deposition temperature of T = 32 K has also been previously demonstrated.[61] Similarly, trapping isolated 1:1 I_2-Xe complexes in solid Kr can be obtained using the same deposition temperature (T = 40 K) and Xe/Kr = 1/1000, I_2/Kr = 1/2600 ratios.[85,A3,III] The matrix preparation parameters for I_2 and I_2-Xe in solid Kr have been studied extensively by Kiviniemi *et al.*, and it has been demonstrated that the preparation technique is very robust in producing repeatable monomeric matrices of high optical quality.

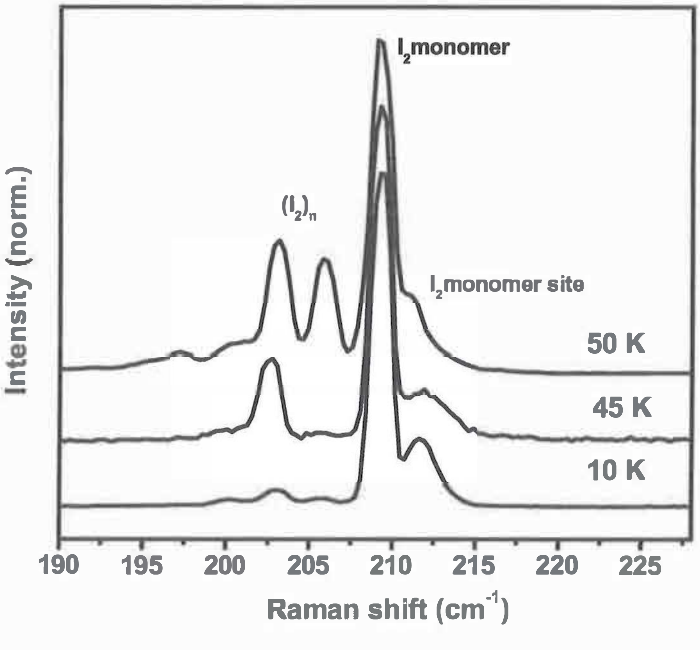

Figure 4-1 Resonance Raman spectra of I_2/Xe samples with different matrix deposition temperatures. The spectra have been measured near the I_2 fundamental after cooling the solid sample to T = 10 K. Monomeric I_2 in solid Xe can be identified from the intense Raman transition at ≈ 209 cm^{-1}. Additional red-shifted transitions (≈ 200–206 cm^{-1}) at higher preparation temperatures (T = 45 K and 50 K) belong to the I_2 aggregates.[III] The blue-shifted transition at ≈ 211 cm^{-1} most likely belongs to an iodine molecule in a vacancy defect site.

Unfortunately, in the case of pure Xe as a matrix for I_2, we have not been able to optimize the sample preparation technique in a way that optically high-quality matrices with purely monomeric trappings of I_2 could be produced. The deposition temperature T = 10 K yielded completely monomeric I_2 trapped in solid Xe. However, the apparent monomericity at this temperature can only be obtained at the expense of optical quality. On the other hand, optically good I_2/Xe matrix samples can be produced at T = 50 K and T = 45 K, although using higher deposition temperatures results in partially aggregated I_2 molecules, as verified by the high-resolution Raman measurements shown in Figure 4-1. Iodine in solid Xe also appeared to exhibit Xe vacancy defects at all tried temperatures.[I] Our MD simulations suggest that Xe vacancies are localized in the 90° angle from the bond axis in the first solvation shell surrounding the I_2 molecules.[I,139] This triple substitutional monomer site in a solid fcc Xe lattice appears to be very stable and independent of sample-preparation parameters (deposition temperature, deposition rate). Similar site defect effects have also been observed for I_2 in solid Ar.[54]

4.2 Gold nanoparticle preparation

Optical and IR measurements were done on essentially *homodisperse* Au_{102}(p-MBA)$_{44}$ samples prepared and purified by Prof. Kornberg's group in Stanford. The synthetic route to purified Au_{102} has been described in more detail in a separate publication by the group,[121] and was also reviewed in publication IV. The synthesis follows closely the two-step method initially proposed by Brust *el al*[102] (see schematic reaction equations (2-8) and (2-9)). Briefly, Au_{102}(p-MBA)$_{44}$ particles are prepared by combining p-MBA and $HAuCl_4$ (p-MBA/Au = 3/1) in a water-methanol solution and stirring the sample for 1 hour. The $NaBH_4$ solution is then added to the mixture and the reaction allowed to proceed for a minimum of 5 hours. The impure product (Au_{102}(p-MBA)$_{44}$ + Au_n(p-MBA)$_m$) is then precipitated with ammonium acetate and methanol. The product is purified by repeated fractional precipitation using ammonium acetate and methanol, as described in Ref. [121]. The *homodispersity* (the presence of pure Au_{102}(p-MBA)$_{44}$) of the samples was studied using X-ray crystallography, photoelectron spectroscopy, mass spectrometry, electron microscopy, thermogravimetric analysis, and PAGE[121] prior to the absorption measurements presented in publication IV. All of the mentioned techniques suggested that the prepared sample is essentially pure Au_{102}(p-MBA)$_{44}$. This is a very crucial notion for the spectroscopic measurements of the Au_{102}(p-MBA)$_{44}$, where impurities in the sample (the presence of other clusters) will hamper the accurate determination of the fundamental spectroscopic properties. Ligand exchange of p-MBA thiols was obtained by reacting equal volumes of purified Au_{102}(p-MBA)$_{44}$ with glutathione (GSH).

The pure Au_{102}(p-MBA)$_{44}$ samples for spectroscopic studies were prepared by dissolving the solid-phase sample to H_2O or D_2O with various concentrations (c = 0.020 - 3 mmol/l). The solid samples of Au_{102}(p-MBA)$_{44}$ and the ligand-exchanged Au_{102} samples were prepared from highly concentrated H_2O solutions by placing a drop of solution on a CaF_2 window and evaporating the it under mechanical vacuum conditions. The sample preparation produces an amorphous-like solid sample with small traces of the solute (H_2O) trapped inside. Alternatively, the same drop-casting procedure was performed in a small aluminum cup suitable for photoacoustic measurements, and on a gold mirror suitable for far-IR measurements.

4.3 Spectroscopic techniques

Stokes-branch resonance Raman measurements in publications I and III were carried out with a home-built backscattering Raman spectrometer with two resolutions: ≈ 1 cm^{-1} and ≈ 5 cm^{-1}. Measurements were made using a frequency-doubled single-mode CW Nd:YAG laser (Alphalas) with a central wavelength at 532 nm. A 50 cm focal-length spectrograph (Acton SpectraPro 2500i) combined to a charge-coupled device (CCD) detector (Andor Newton) was used to detect the Raman and the emission signals. The laser line (Rayleigh) was suppressed using an edge filter (Semrock). In publication I, visible absorption was also detected using the Raman instrument described above with a stable light-emitting diode (LED, white-light) as a light source.

The detection system used to gather the absorption, emission and pump-probe measurements presented in publication II was constructed from an image-intensified-CCD (Andor) and a 12.5 cm focal-length spectrograph (Oriel MS 125), time-gated with a delay generator (Stanford Research Systems). A D_2-lamp (Cathodeon) was used as a VUV/UV light source in the absorption measurements. In VUV measurements the light path and the detection system were efficiently purged with a nitrogen (N_2) gas flow. Steady-state LIF measurements of the I_2/Xe/Kr ternary systems were recorded after 193 nm excitation with an ArF excimer laser (Optex), with an average pulse length of 5-10 ns.

The TRCARS and pump-probe measurements in publication II were gathered using three home-built non-collinear optical parametric amplifiers (NOPA), or alternatively with a commercial OPA (TOPAS, Light Conversion Ltd.). The parametric amplifiers were pumped by an integrated femtosecond Ti: sapphire laser (Coherent Libra), with a ~1 mJ output at 800 nm (repetition rate 1 kHz). The generated optical region near-transform limited fs-pulses were delayed using a computer-controlled delay line (Aerotech). The temporal widths of the pulses were approximated by autocorrelation measurements (typically ~50–100 fs). A cooled photomultiplier tube (PMT) was used to detect a spatially and spectrally filtered coherent CARS signal. An incoherent spectrally resolved pump-probe signal was detected using the time-gated ICCD described above. The experimental TRCARS setup and the theoretical background for polarization-beat spectroscopy are described in detail in Refs. [61] and [85].

Mid-IR-NIR-absorption measurement of solid- and liquid-phase Au_{102}(p-MBA)$_{44}$ samples were conducted using a commercial FTIR spectrometer (Nicolet Magna 760) equipped with a nitrogen-cooled mercury-cadmium-telluride (MCTB) detector. The solid-phase samples were additionally measured using a commercial photoacoustic detector (Gasera PA301) connected to a FTIR spectrometer. The physical basis and the experimental realization of cantilever-based FTIR photoacoustic detection can be found in Ref. [140] and the references therein. Far-IR measurements of $Au_{102}(p\text{-MBA})_{44}$ were conducted at the MAX-lab synchrotron facility in Lund using a Bruker IFS 120 HR far-IR instrument (globar far-IR source, Mylar beamsplitter) equipped with a He-bolometer detector. The spectra were measured from solid-phase samples located on top of a gold mirror kept at T = 4.8 K inside a He-flow cryostat (Janis Research Co.).

5 RESULTS AND DISCUSSION

The results presented in this chapter summarize and highlight some of the key results discussed in more detail in publications I-IV.

5.1 Signatures of I_2 in solid Xe

5.1.1 Vibronic B↔X ZPLs and PSBs

Iodine B↔X transition in solid Xe was studied using linear absorption and laser-induced emission.[I] Figure 5-1a shows the absorption spectra of a crystalline I_2/Xe sample directly after sample preparation at T = 45 K and cooling to T = 10 K. The appearance of a prominent vibronic structure in the 16500-18000 cm^{-1} region of the B←X absorption is clearly observable in the 10 K spectrum. The structures appear at approximately the energy region where transitions to the bound portion of the B-state are expected in the gas phase, as shown by the comparison with the B←X gas-phase molar absorption coefficient envelope by Telllighuisen (red spectrum).[36] The inset in Figure 5-1a is a magnification of one of the vibronic B←X transitions. With our suggested numbering, this is the v′(B)=20 ← v″(X)=0 transition.[I] All vibronic structures at the 10 K spectrum have a very distinctive bimodal structure with a sharp lower-energy peak and a broader higher-energy band. The double-band structure corresponds to a molecular ZPL (sharp Lorentzian line) and the simultaneous excitation of broad-range phonon modes of the I_2/Xe system (PSB). The impulsive excitation of the I_2/Xe phonon modes, along with the molecular vibronic transition, generates the broad PSB on the blue energy side of the ZPLs (see Section 3.2). Very similar ZPL + PSB vibronic structures have been reported for the B-state excitation spectra of Cl_2[133] and Br_2[128,132] in low-temperature Ar matrices, but not for the I_2.

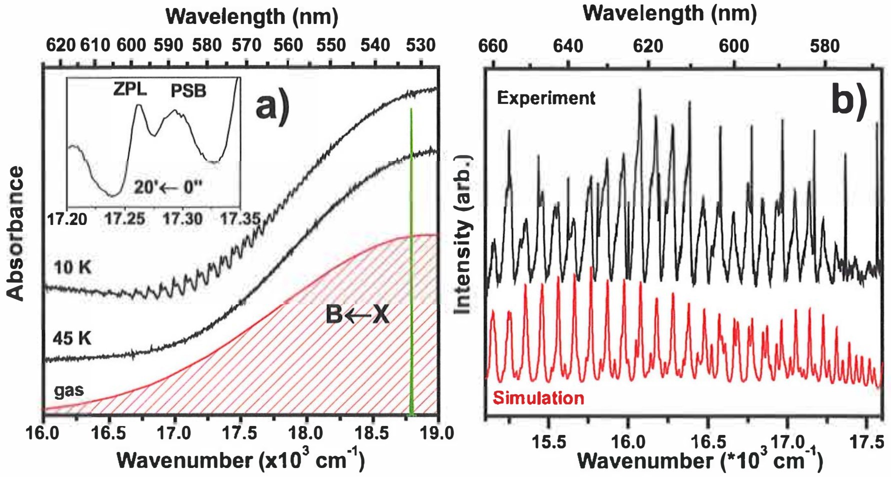

Figure 5-1 (a) Absorption spectra of I_2/Xe at T = 45 K and T = 10 K in comparison with a gas-phase molar absorption coefficient envelope by Tellighuisen.[36] (b) Experimental hot luminescence/Raman spectrum of the same sample at T = 10K showing the vibronic structures in B-state emission (black spectrum). F-C simulation of the hot luminescence (red spectrum).

The phonon coupling strength of the chromophore (I_2) and the bath (Xe environment) shows a strong increase as the higher vibrational states on the excited electronic state are reached. A similar type of increasing phonon coupling strength as a function of B-state vibrational quantum is also observed for Cl_2 and Br_2 in Ar.[128,134] Interestingly, the excited phonon modes in the PSB become more localized further from the ZPLs when higher B-state v'-states are excited. At the highest observed excitations (~30'←- 0''), the excited phonon modes are localized near the Debye cut-off frequency of solid Xe (≈ 44 cm^{-1}).[50]

The presence of I_2 vibronic ZPLs in low-temperature solid Xe enables the parameterization of the B-state electronic potential using a normal Birge-Sponer analysis.[43] The suggested experimental spectroscopic parameters for the B-state are: ω_e = 120.2 cm^{-1}, $\omega_e x_e$ = 0.60 cm^{-1}, $\omega_e y_e$ = -0.006 cm^{-1} and T_e = 15200 cm^{-1}.[I] The harmonic frequency shows a notable reduction from the gas-phase value[29] ($\Delta\omega_e$ = -5.1 cm^{-1}) in solid Xe. The potential origin T_e of the B-state is expectedly red-shifted from the gas-phase value ($\Delta T_e(B)$ = -570 cm^{-1}). A similar shift is also observed for the A-state in solid Xe ($\Delta T_e(A)$ = -507 cm^{-1}).[57]

Vibronic structures observed in the linear absorption spectrum are observable in the non-relaxed emission from the B-state as shown in Figure 5-1b. The hot luminescence phenomenon from the relaxing B-state populations has been reported in different RGs[101] and in liquids.[141,142] However, in solid Xe (T = 10K) the emissions are highly structured, as shown in Figure 5-1b which depicts the portion of the hot luminescence spectrum obtained with 532 nm excitation (the laser line is shown in panel a). By comparing the experimental transitions to a Franck-Condon intensity simulation (red spectrum Figure 5-1b) of the B→X transitions, we established that the observed emissions (ZPLs) originate from various B vibrational states to primarily the lowest vibrational states on the ground electronic state (v'' = 0-4).[I] The studies of Böhling *et al.* in solid Xe do indeed show that the relaxed emissions from the A-state contain plausibly zero-phonon line (ZPL) contributions, further confirming the assignment of I_2 ZPLs in solid Xe.[51]

5.1.2 Long-lived electronic coherence

The vibronic structures in the B←X absorption shown in Figures 5-1a and 5-2a are a direct manifestation of *electronic* coherence that outlives the vibrational period of the excited-state molecule in the low-temperature I_2/Xe system. Estimation of the lower limit of the electronic dephasing time can be deduced directly from the energy-space linewidths of the vibronic transition in the absorption spectrum (see equation 3-2). The lower limit of the electronic dephasing time (T_2) for B←X transition of I_2 in solid Xe varies between 0.4-1.8 ps in the observed range of vibrational states (v' = 10-31).[I]

In order to get more insight and highlight the long-lived electronic coherence, Panel b of Figure 5-2 shows the Fourier transform of the vibronic absorption spectrum in Panel a. The Fourier transform of the absorption signal can be considered to yield the many-body quantum correlation function *C(t)* of wave packet evolving on the B-state[124,126] The time-domain signal shows the recurring evolution of the I_2/Xe B-state wavepacket on the time scale of ≈ 360 fs, correlating with the average energy separation of the vibronic transitions in the energy spectrum and the B-state vibrational period. The time-domain signal also shows how a rather large portion (20%) of the wavepacket reaches the initial overlap after the first round trip on the B-state, and several recurrences are clearly observable up to ≈ 1.6 ps.

As stated in Section 2.1.2, the *vibrational* coherences generated in the I_2 B-state in Ar and Kr are known to decay in time scales of few picoseconds (see for example, the pump-probe spectra in Figure 2-8). However, the absorption spectrum of I_2, which probes directly the electronic part of the coherence, is rather peculiar in low-temperature Xe. This because no similar vibronic signatures have been reported in the literature for any *condensed*-phase environment for I_2, despite the fact that this particular transition has been under very intense study in all possible phases and environments. Nonetheless, Jungwirth *et al.* have shown that wavepacket recurrences occur in full quantum simulations of Raman processes in large I_2-Xe_n clusters,[143] and more interestingly, the authors suggest that such processes are even more prominent in solid Xe, an assumption now proven correct in the present study. It can be tentatively suggested that the likely reason for the long-lived electronic coherence is iodine's inability to displace heavy Xe atoms during the collision of the vibrating molecule and the caging RG atoms in the excited B-state. However, the question of why ZPLs and PSBs are present only in solid Xe is still fully open, and further studies of this interesting condensed-phase model system are clearly needed.

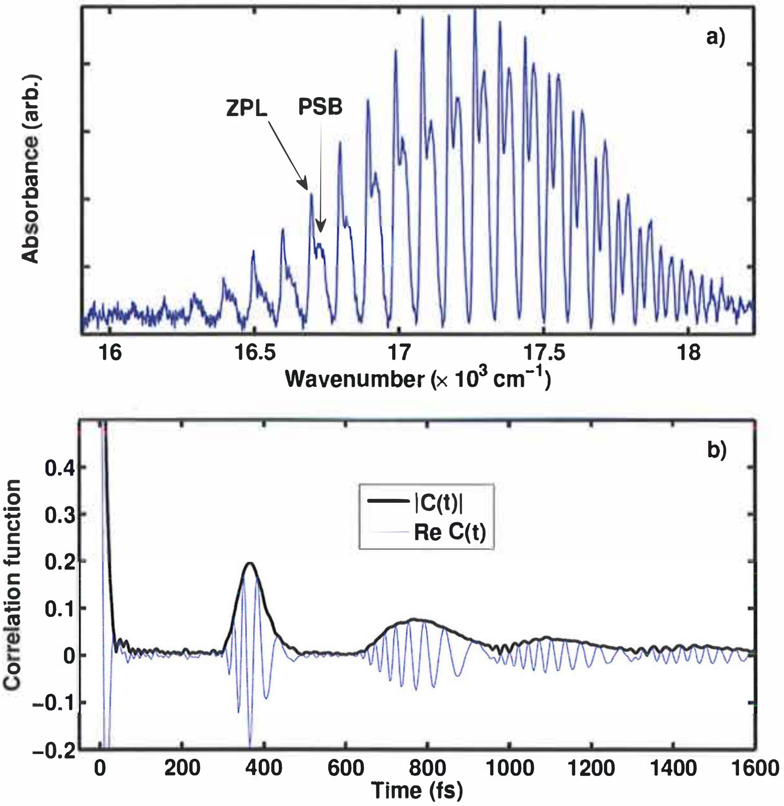

Figure 5-2 (a) Base-line corrected absorption spectra of I_2/Xe (T =10 K) (b) Fourier transform of the absorption signal in the top panel, showing the absolute magnitude and the real-part of the many-body correlation function C(t). Reproduced from Ref. [139] (unpublished) .

5.2 Signatures of I_2-Xe complex in solid Kr

5.2.1 VUV absorption and emission

The electronic transition signature for the I_2-Xe complex was found in the vacuum ultraviolet (VUV) absorption of ion-pair states in solid Kr.[II] Figure 5-3 depicts the absorption spectra of solid I_2/Xe/Kr ternary systems, where the number (Xe = n%) is the percentage of Xe gas in the initial gas phase (I_2/Kr = 1/2600) sample used to prepare the solid-phase crystalline samples. The VUV absorption spectra of D←X transition[49] (see also Figure 2-3) showed strong systematic red-shifting behavior from the pure Kr case (Xe = 0%) as a function of Xe percentage. The red-shifting effect is clearly visible even with trace amounts of Xe. This can be understood as the appearance of a new absorption band at ω = 51200 cm^{-1}, induced and enhanced by the Xe presence in the sample. Figure 5-3 highlights qualitatively the appearance of the new absorption band in the VUV region with a dark-blue color and the disappearance of the I_2/Kr D←X transition with a red color. Notably, the Xe-induced band already completely dominates the absorption spectrum with a doping level of Xe = 0.5%.

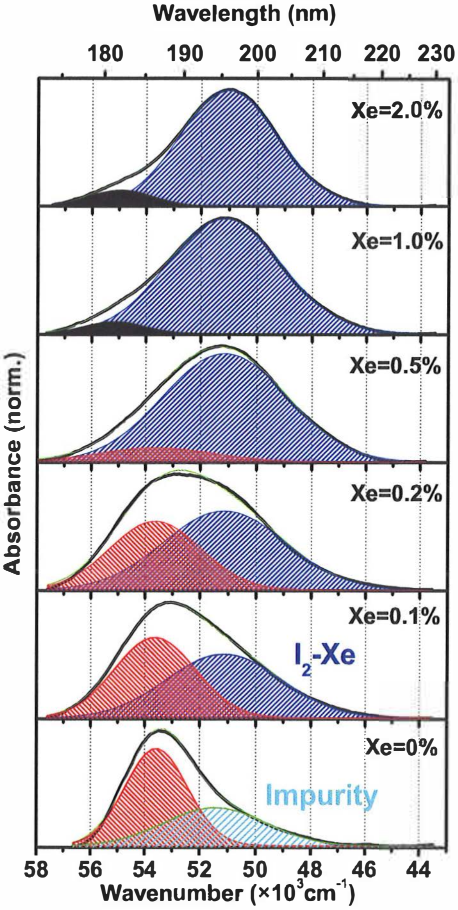

Figure 5-3 VUV absorption spectra of I_2/Xe/Kr ternary systems at T = 40 K with varying Xe percentage. Adapted from publication II. Copyright © 2012 American Institute of Physics.

The Xe doping levels in Figure 5-3 typically yield solid Kr matrices where isolated 1:1 I_2-Xe complexes have been previously observed.[85,A3] The presence of isolated I_2-Xe complex in the Xe = 0.1% case was verified using the polarization beats in the TRCARS traces.[II] The previously reported results and the verification of the complex presence in Xe = 0.1 % sample strongly suggest that the Xe-induced absorption in the VUV region (the blue band) belongs to the 1:1 I_2-Xe complex in solid Kr, thus identifying a novel spectroscopic signature for the van der Waals complex in electronic spectroscopy.

Interestingly, the I_2-Xe complex could not be directly observed in the relaxed emission from the ion-pair states. Figure 5-4 shows the emission spectra from various ion-pair states as a function of Xe percentage. The spectra are measured after direct excitation of the D-state using ArF excimer laser (193 nm). Excitation of the I_2 D-state in solid RGs[49] and in the gas-phase rare gas clusters[80] leads to a rapid environment-mediated population relaxation through the ion-pair tiers and subsequent emission from multiple terminal ion-pair states. Emissions with 193 excitation mainly originate from the first ion-pair tier (namely from IP states D′ and δ). However, emissions presumably from the second IP tier can also be observed (from IP states f and F). Relaxed emissions show a typically short life-time of approximately 20 ns. All observed emissions in the Xe-doped cases can be attributed to emissions from I_2 IP states, without evidence of distinct transitions belonging to the complex. Nonetheless, dramatic relative-intensity drops from the first IP tier can be observed in the steady-state emission spectra of Xe-doped matrices. Figure 5-4 shows the intensity changes (compared to the second IP tier emission F→a′) as a function Xe doping.

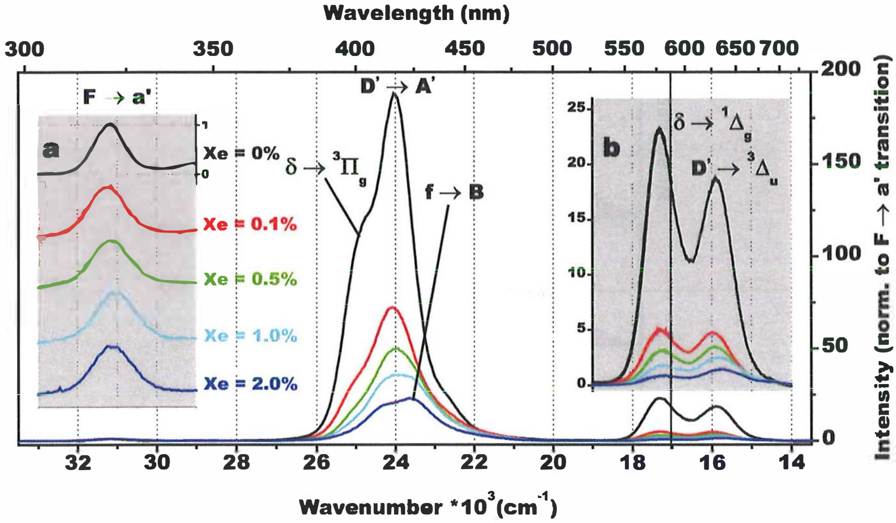

Figure 5-4 Emission spectra of I_2/Xe/Kr ternary systems with the same Xe-doping ratios as in Figure 5-3. Panels (a) and (b) highlight the weaker features of the spectra. Tentative assignments of different transition are shown in the figure. From publication II. Copyright © 2012 American Institute of Physics.

The intensity-drops can be understood as efficient predissociation of the first IP-tier states to the doubly spin-excited valence states (I*-I*) upon complexation of the I_2 molecule in solid Kr, similarly to the pure Xe case.[144] However, this relaxation path can only be weakly observed in the lowest Xe-doping ratios. Therefore, further studies of the isolated complex are necessary to fully confirm the relaxation channels for the complex from the IP manifolds. Also, the pump-probe studies utilizing the B- and the A-states as an intermediate step show no direct indication of the complex in the time-domain signals or in the relaxed emission from the different IP states used as a probe in these experiments.

5.2.2 Symmetry breaking of IP states

The appearance of a new absorption in the VUV-region upon complexation of I_2 with Xe is clear in Figure 5-3. We are tentatively proposing that this new complex state is effectively the I_2(D) IP state, in which the inversion symmetry of the state (see Equation 2-1) is broken by the close interaction with the Xe atom. This leads to a state with a permanent dipole and strong instantaneous solvation of the state by the Kr environment (see Equation 2-5). The effect induced by the complexation would be very similar to what was observed in the relaxed emission of I_2 IP states (D′ and δ) in solid RGs. In these studies, where Yu and Coker[42] simulated the experimental results of Helbing and Chergui,[49] the environmentally mediated (distortion of the matrix cage) symmetry breaking of the I_2 IP states was used to explain the strong solvation shifts of the IP states in relaxed emission in solid RGs (Ar, Kr)—an effect apparently absent in the VUV absorption.[49] In our case, however, the relaxation would not be necessary, due to the presence of a ground-state complex which will break the symmetry of the IP states directly in absorption. It can also be suggested that this phenomenon would only be observable in an asymmetric complex, where unequal interaction with the different I atoms of the molecule is necessary to break the symmetry of the IP state. Thus the symmetry breaking would further indicate a linear complex in solid Kr, as has already been argued based on the higher stability of the linear complex compared to the T-shaped complex.[85]

However, it must be stated that the exact nature of the complex transition is not fully understood at present. Another plausible explanation for the transition would be a direct charge-transfer (CT) transition between I_2 and Xe, which can be expected to be very close in energy to the I_2 first IP tier in solid Kr,[42, 80] similar to the I_2-benzene complex.[A1,A2] The two different mechanisms are illustrated in the following schematic equations, where Equation (5-1) illustrates the symmetry-breaking of the I_2 D IP state and Equation (5-2) the charge-transfer between complex partners.

$$I_2 - \mathrm{Xe} + h\nu \rightarrow {}^{\delta-}I_2{}^{\delta+} - \mathrm{Xe} \tag{5-1}$$

$$I_2 - \mathrm{Xe} + h\nu \rightarrow I_2{}^{-} - \mathrm{Xe}^{+} \tag{5-2}$$

Both presented mechanisms lead to states with a permanent dipole, which is strongly and instantaneously solvated (red-shifted) in the Kr environment. Thus, for definite assignment of the nature of the VUV absorption for the complex, more experimental and theoretical studies are needed. However, this will not change the fact that the electronic transition at $\omega = 51200$ cm^{-1} most likely belongs to the I_2-Xe complex in solid Kr. The strongly red-shifted VUV-absorption of I_2 in pure solid Xe (see Figure 2-6b, Xe) is also a very interesting result. The red-shifting suggests that symmetries of the I_2 IP states are broken in the Xe environment, even though a highly symmetrical solvation environment is apparently restored.

5.3 Signatures of I_2 clusters in solid Kr

5.3.1 Cluster formation observed by Raman spectroscopy

Figure 5-5a summarizes the experimental findings in publication III by showing two resonance Raman spectra of the same solid I_2/Kr sample at two different temperatures T = 32 K and T = 54 K. The experimental high-resolution Raman spectra (black and red spectra) are measured near the Raman fundamental transition of I_2 in solid Kr. The black spectrum is measured directly after sample preparation at T = 32 K, and the red spectrum after the slow annealing of the same sample (1 K/min) to T = 54 K. The initial black spectrum shows only signal from the isolated monomeric I_2 molecule in solid Kr (211cm^{-1}).[61] The annealed spectrum (T = 54 K) shows multiple additional Raman transitions belonging to the small I_2 clusters (198-205 cm^{-1}) and the bulk-like I_2 species, as indicated in Figure 5-5a. The presence of bulk-like I_2 can be identified from the T = 54 K spectrum by the appearance of the intense Raman doublet (181 cm^{-1} and 190 cm^{-1}), closely resembling the fundamental transitions observed for the bulk crystalline I_2.[48]

The small I_2 clusters in the 198-205 cm^{-1} region are formed by aggregating thermally mobilized monomers inside the crystalline Kr lattice. Figure 5-5b shows the relative integrated intensity of the monomer band (211 cm^{-1}) compared to the integrated intensity of the whole cluster region (198-205 cm^{-1}) as a function of temperature. The systematic relative increase of the cluster intensity compared to the monomer intensity establishes that the small clusters are formed by aggregating monomers in the temperature range T = 45-55 K. At higher temperatures (T > 52 K) the direct formation of bulk-type I_2 species dominates the thermally induced cluster formation kinetics (possibly assisted by laser heating).

The most intense (red-shifted) Raman fundamental frequencies for $(I_2)_{2-7}$ clusters, predicted by our DFT D level electronic structure calculations, are shown in comparison with the experimentally observed transitions in Figure 5-

5a (colored vertical lines). The calculated monomer fundamental (*n* = 1) is depicted with a black vertical line; the cluster transitions are identified by the colored numbering, indicating the number of I_2 molecules in the complex (n = 2-7). The calculated Raman fundamentals of I_2 clusters are grouped in two distinct type of transitions (highlighted with black boxes): Transitions which are red-shifted ≈ 10 cm^{-1} (198-205 cm^{-1}) and transitions which show much stronger red-shifting of ≈ 20 cm^{-1} from the monomer transition. The two-stage red-shifting behavior of the Raman transitions is intimately related to the size and the structure of clusters. The structural aspect of the red-shifting will be discussed in the next section.

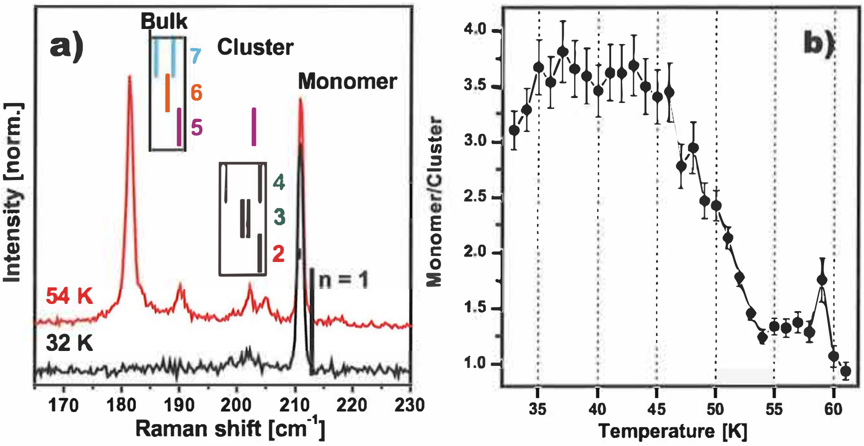

Figure 5-5 a) Raman spectra of I_2/Kr sample at T = 32 and after annealing to T = 54 K (for an explanation of the colored lines, see text); b) Relative integrated intensity of the monomer band compared to the cluster region (198-205 cm^{-1}). Adapted from publication III. Copyright © 2009 American Chemical Society.

The first stage of red-shifting (ca. 10 cm^{-1}) appears for the smallest calculated I_2 clusters, namely clusters $(I_2)_{2\text{-}4}$. These three different cluster contributions can be resolved and identified in the Raman spectrum by closer inspection of the relative intensities as functions of temperature in the 198-205 cm^{-1} region.[III] The second stage of red-shifting (ca. 20 cm^{-1}) is expected only for the larger clusters with *n* ≥ 5, as shown in Figure 5-5a.

The key to the successful observation of the small cluster species in the Raman spectrum of I_2-doped solid Kr is the instrumental resolution (≈ 1 cm^{-1}) and the controlled thermal mobilization of the I_2 monomers in the lattice. However, the I_2 clusters can also be readily observed in solid Xe, as was shown in Figure 4-1.

5.3.2 Structural motif of the crystalline I_2 in small clusters

Optimized gas-phase I_2 cluster geometries from dimeric (2) to heptameric (7) iodine clusters are represented in Figure 5-6. All DFT-D-level optimized structures have planar-cluster geometry, and the complexes are confined in the b-c plane of the crystalline iodine lattice (see Figure 2-1). The numbers indicate the number of I_2 molecules in the cluster, and the calculated Raman transitions in Figure 5-5a (colored lines) correspond to the structures shown in Figure 5-6. The emergence of a molecular packing orientation of the crystalline structure is qualitatively visible in the calculated minimum energy structures. The I_2 bond distances (R_{I2}) show ≈ 70% of the bond elongation from the gas-phase molecule ($R_e(g)$ = 2.666 Å[22]) to the bond length in a bulk solid ($R_e(s)$ = 2.715 Å [18]) in the calculated range of $(I_2)_n$ clusters (n = 2-7). The closest intermolecular distances (R_{vdW}) show near convergence to the crystal structure in the same range of cluster sizes. Similarly, approximately 60% of the total lattice energy (-63.8 kJ/mol)[23] is already covered in the largest heptameric cluster.

The calculated Raman transitions in Figure 5-5a indicate that the transition energies show a similarly fast convergence to the two bulk-type Raman transitions in the small clusters. The origin of the two-stage shifting of Raman transitions in I_2 clusters becomes evident by inspecting the cluster structures in Figure 5-6. The first stage of the Raman shift (≈ 10 cm^{-1}) is only observed in clusters with n = 2-4. The most red-shifted Raman frequency is always localized in the central I_2 molecule, which shows only partial coordination to the other molecules up to n = 4 (the other end of the molecule is practically free). The second stage of red-shifting (≈ 20 cm-1) is observed in the calculated spectra when the fifth molecule is added to the cluster (n = 5). In this case the central molecule shows full coordination from all directions. The full coordination is thus associated with the large red shift observed in clusters with n > 4.

The small iodine clusters show structurally and spectrally fast transitions from the isolated molecule limit to clusters with bulk crystal-like properties.

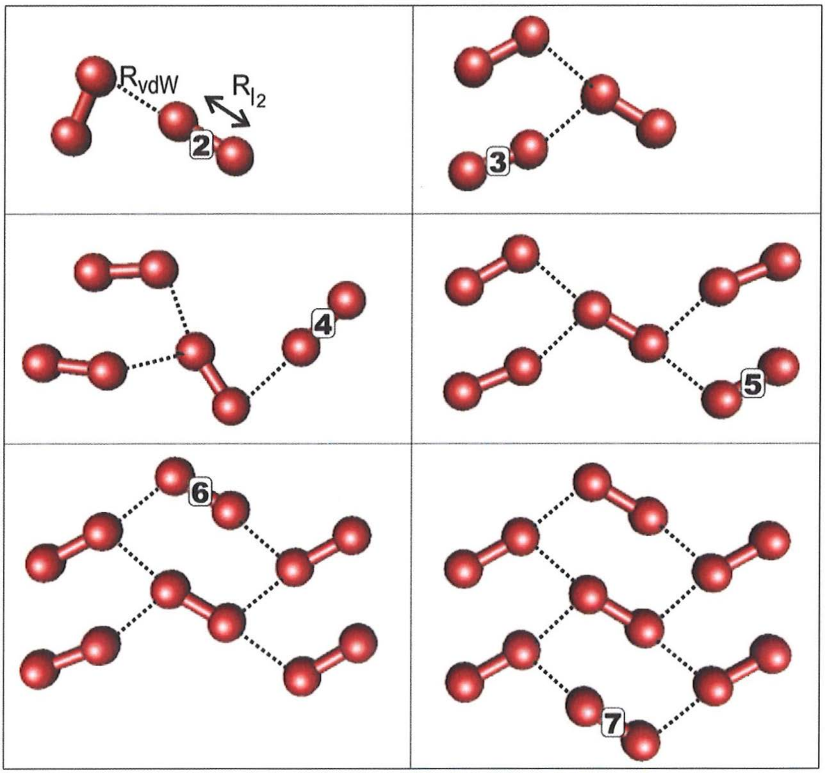

Figure 5-6 Optimized $(I_2)_n$ (n =2-7) cluster geometries at the DFT-D level of theory with P3LYP parameterization of the exchange-correlation functional. The horizontal and the vertical axes represent the *b* and *c* crystalline axes of the solid I_2 lattice. From publication III. Copyright © 2009 American Chemical Society.

5.4 Signatures of Au_{102}(p-MBA)$_{44}$ in the condensed phase

5.4.1 Electronic and vibrational signatures

Absorption spectra of Au_{102}(p-MBA)$_{44}$ nanoclusters were measured from H_2O and D_2O solutions and thin films of solid-phase samples at room temperature. The absorption spectra were measured in the mid-IR to UV region (0.2 - 6 eV) from the liquid-phase samples, and in the mid-IR to near-IR (1-0.04 eV ≈ 8000-400 cm^{-1}) in solid-phase samples. Solid-phase samples were also recently measured in the far-IR region (140-600 cm^{-1}) at T = 4.8 K.[121] All spectroscopic measurements were done on *homodisperse* Au_{102}(p-MBA)$_{44}$ samples prepared and purified by Prof. Kornberg's group (see Section 4.2).[121] The experimental absorption results were compared to a theoretically calculated absorption spectrum of Au_{102}(SMe)$_{44}$ model cluster, obtained at the LR-TDDFT level of theory using the known structure of the Au_{102}(p-MBA)$_{44}$.[106]

Figure 5-7 shows the experimental electronic absorption spectra (red line, main picture, inset A) of a purified Au_{102}(p-MBA)$_{44}$ in a room-temperature H_2O solution. The lowest portion of the spectrum ≈>0.5 eV is measured in D_2O solution instead of H_2O, to avoid the strong -OH stretch vibration (≈ 3200 cm^{-1}) contributions to the absorption spectrum in the low-energy region. The blue line in the main picture of Figure 5-7 is the calculated spectrum of the model cluster (see Figure 2-12). Note that the absolute molar absorption coefficient scale for the experimental and the theoretical spectrum are the same. Both spectra show four clearly distinguishable absorption features in 1.5–3.5 eV region marked with Roman numerals in the theoretical spectrum. These absorption features are reproduced in different measurements of the cluster, and the structures are attributed as the electronic signature features of the Au_{102}(p-MBA)$_{44}$ cluster.

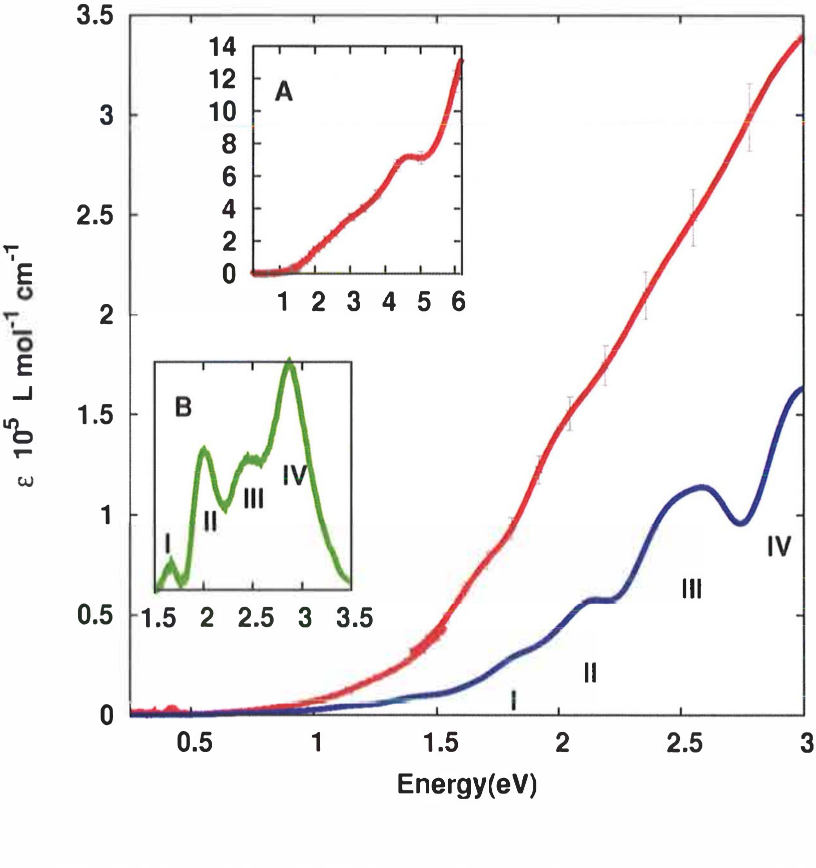

Figure 5-7 Main picture) Molar absorption coefficients of the Au_{102}(p-MBA)$_{44}$ nanocluster in H_2O/D_2O solutions in the visible region. (A) Full absorption spectrum from mid-IR to UV. (B) Baseline corrected absorption spectrum highlighting the weak absorption features (I-IV). From publication IV. Copyright © 2012 American Chemical Society.

The positions of experimental electronic signature features are highlighted in Panel B of Figure 5-7, where the dominant unresolved absorption background is removed in the 1.5–3.5 eV region by arbitrary baseline correction with a linear function. This procedure merely emphasizes the absorption features otherwise difficult to observe. The spectrum also confirms that cluster does not exhibit plasmon resonance at 520 nm (≈ 2.4 eV) expected for larger clusters and colloidal gold.[119]

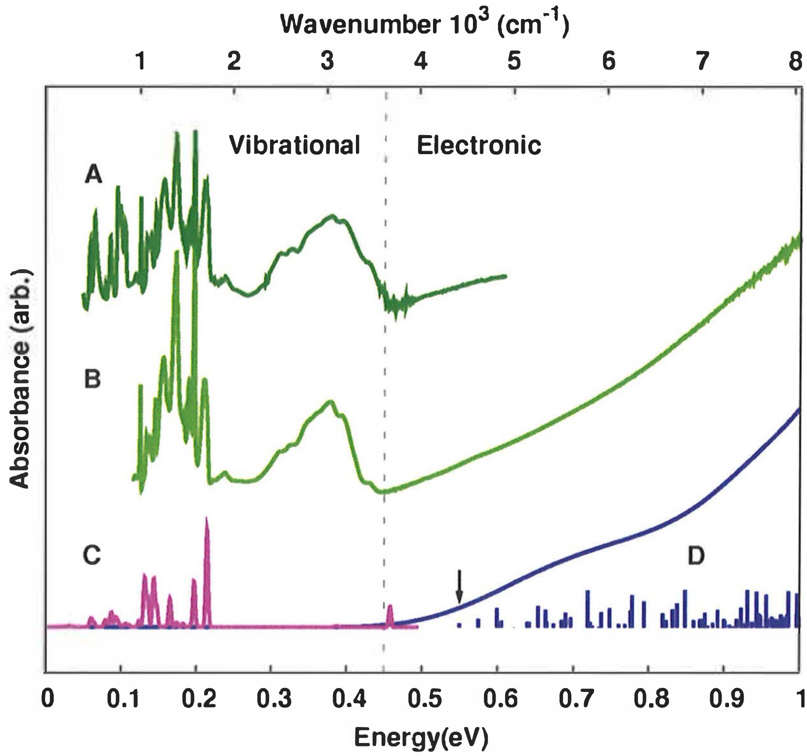

Figure 5-8 Experimental and theoretical absorption spectra of the $Au_{102}(p\text{-}MBA)_{44}$ cluster in the NIR region (A) FTIR spectrum using photoacoustic detection (B) transmission FTIR (C). Calculated IR spectrum of single p-MBA thiol (D) Absorption spectrum from LR-TDDFT calculation (stick spectrum) and the convoluted spectrum (blue line). From publication IV. Copyright © 2012 American Chemical Society.

The onset of electronic transitions is established experimentally by FTIR measurements of solid-phase $Au_{102}(p\text{-}MBA)_{44}$ samples prepared as described in section 4.2. Figure 5-8 shows the experimental spectra obtained by two independent measurements. The A and the B spectra are FTIR measurements using a photoacoustic detector (A) and a normal transmission geometry measurement through the solid sample with a liquid-nitrogen-cooled MCTB detector (B). Clear onset of electronic transitions can be seen in all experimental spectra at 0.45 ± 0.5 eV (dashed line). Results agree extremely well with the calculated electronic onset at 0.55 eV which belongs to a transition localized at the cluster core with a dominantly Au(6sp) to Au(6sp) intraband character (arrow) (see Figure 2-12).

Figure 5-8 also shows the distinction between the vibrational transitions of p-MBA-thiol layer and the electronic transitions of the cluster. The sharp transitions in the ≈ 0.2-0.04 eV region are different ligand vibrations, as shown by the comparison with the theoretical spectrum of single p-MBA thiol (C). The broad transition at the ≈ 0.3-0.4 eV region consists of hydrogen-bonded carboxylic acid -OH vibrations and -OH vibrations of trapped water in the cluster. Interestingly, when ligand exchange is performed for the Au_{102}(p-MBA)$_{44}$ cluster using GSH, a clear indication of partial exchange can be observed in the vibrational region, but the onset of electronic transition is not notably affected.[IV]

Figure 5-9 shows the far-IR region of the vibrational spectrum of Au_{102}(p-MBA)$_{44}$.[145] The transitions with energy above 400 cm^{-1} have been previously observed in photoacoustic measurements of room-temperature samples.[IV] Our recent DFT calculations of the staple units (short and long staple units connected to two gold atoms mimicking the core of the cluster) suggest that the weak transitions below 400 cm^{-1} are vibrational modes involving Au-S stretch character. The calculated Au^{I}-S stretch vibrations of the two staple units are localized in the ≈ 320 – 380 cm^{-1} region. The experimental spectrum shows also a clear IR-band in this region. According to the calculation, the lower-energy region (≈ 190 – 320 cm^{-1}) contains vibration modes involving the Au-core (in the calculation of two fixed Au atoms) and the ligand units. Similar results have been obtained in previous studies of alkanethiolate-protected clusters where Au-S stretch vibrations have been observed in the 170–270 cm^{-1} region.[146] The vibrational transitions above 400 cm^{-1} are ligand vibrations (involving bending motion). Interestingly, the calculation predicts that the asymmetric shapes of the transitions above 400 cm^{-1} most likely originate from two types of ligand units in the Au_{102}(p-MBA)$_{44}$ cluster.

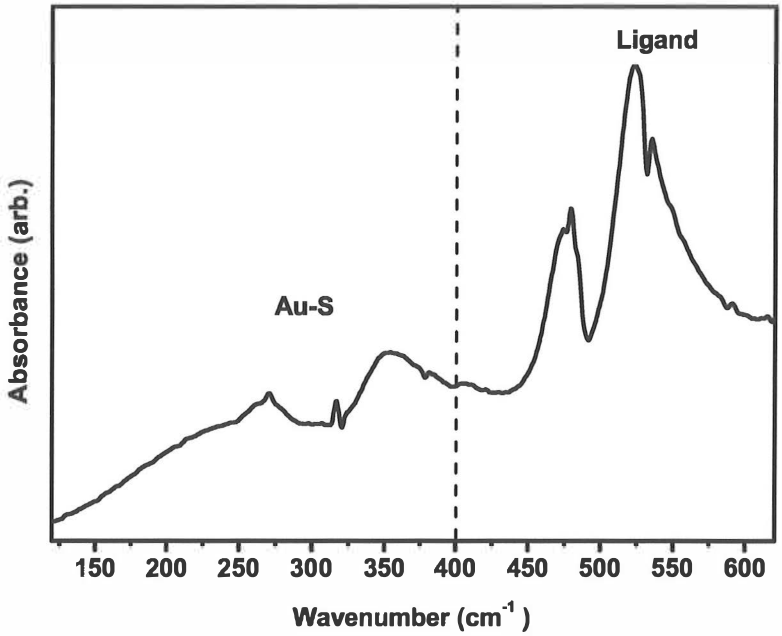

Figure 5-9 Far-IR spectrum of Au_{102}(p-MBA)$_{44}$ measured at T = 4.8 K.

5.4.2 Electronic stability of Au_{102}(p-MBA)$_{44}$

The verified experimental existence of a HOMO-LUMO gap for the Au_{102}(p-MBA)$_{44}$ cluster, and a clear onset of electronic transitions over this band gap at 0.45 eV, establishes that the cluster shows finite-size effects and a molecular-like behavior in the electronic spectroscopy. The existence of an experimental HOMO-LUMO gap strongly suggests that the stability of this cluster must have an electronic origin, besides the structurally stabilizing ligand sheltering effects. The experimental results partially confirm the theoretical prediction by Walter *et al.* of the 58 electron shell closure in this cluster, and the opening of a significant band gap.[107] The absorption results offer a way to indentify the Au_{102}(p-MBA)$_{44}$ using common spectroscopic techniques, which can be used in various applications. The combined experimental results and the calculated spectra of Au_{102}(SMe)$_{44}$ also confirm the effectiveness of the LR-TDDFT description in predicting cluster properties in a fully quantitative manner.

The FTIR result also indicates that the metal core of the cluster is very robust against partial ligand-exchange, which is a very important factor when atomically precise clusters are functionalized for various purposes. The recent far-IR measurement and the DFT calculations suggest a plausible Au-S stretch origin for the very low-energy transitions observed in this cluster. The full spectroscopic characterization of $Au_{102}(p\text{-MBA})_{44}$ is, however, the key result of publication IV. Studies of this intriguing ″superatomic″ nanocluster with accurate atomic composition will most certainly continue in the future. The results presented in publication IV are only a small piece in the puzzle in the attempt to define the unifying principles behind the stability of monolayer-protected clusters and the factors defining their structure. It remains to be seen in the (very exciting) future if the electronic shell closures shown for $Au_{102}(p\text{-MBA})_{44}$ also contribute to larger clusters, and what the extent of electronic stabilization in the "magically" stable Au clusters is.

SUMMARY

Several iodine- and gold-containing molecular, complex, and cluster systems were studied using spectroscopic techniques ranging from far-IR FTIR measurements to vacuum-UV absorption measurements in condensed-phase environments.

Molecular iodine in solid crystalline Xe was found to exhibit vibronic ZPLs and PSBs in the visible region B↔X transition, indicating exceptionally long-lived electronic coherence between the electronic states in the condensed phase. The electronic signature for the isolated 1:1 I_2-Xe complex in solid crystalline Kr was found in the vacuum-UV absorption, with absorption maximum at approximately 51200 cm^{-1}. The electronic transition is suggested to originate from symmetry breaking of the I_2 D ion-pair state in the complex and formation of a permanent dipole state. Vibrational signature features for neutral molecular iodine clusters were found using resonance Raman spectroscopy in solid Kr. Small $(I_2)_{2\text{-}4}$ clusters were found to exhibit ≈ 10 cm^{-1}, and larger clusters $(I_2)_{>5}$ ≈ 20 cm^{-1} red-shifts from the isolated I_2 molecule. The red-shifting behavior in iodine clusters is understood to originate from partial or full coordination of the central I_2 molecule. Iodine clusters show a fast transition from the isolated molecule limit to the mesoscopic bulk limit in terms of the Raman shift and structural properties.

Electronic and vibrational signatures of pure Au_{102}(p-MBA)$_{44}$ gold nanoclusters have been identified using absorption spectroscopy of liquid- and solid-phase samples in a region from far-IR to UV. Au_{102}(p-MBA)$_{44}$ has four electronic signature features in the NIR-visible region and an onset of electronic transitions at 0.45 eV. Vibrational signatures of the ligand layer and the Au-S interface have been observed and partially identified. The ligand exchange of p-BMA thiols in an Au_{102}(p-MBA)$_{44}$ cluster does not notably affect the electronic onset, implying a structurally intact Au core after ligand exchange. The results establish the existence of the theoretically predicted HOMO-LUMO band gap for the Au_{102}(p-MBA)$_{44}$ cluster, suggesting an electronic origin for the stability of the cluster.

REFERENCES

1. Herzberg, G. Spectroscopic Studies of Molecular Structure, Nobel Lecture, Dec 11, 1971. www.nobelprize.org (accessed Aug 16, 2012).

2. Mulliken, R. S. Spectroscopy, Molecular Orbitals, and Chemical Bonding, Nobel Lecture, Dec 12, 1966. www.nobelprize.org (accessed Aug 16, 2012)

3. Häkkinen, H. *Nature Chem.* **2012**, *4*, 443-455.

4. Qian, H.; Zhu, M.; Wu, Z.; Jin, R. *Acc. Chem. Res.* **2012**, DOI: *10.1021/ar200331z*, ASAP.

5. Iodine. Oxford Dictionaries Online. www.oxforddictionaries.com (accessed Jul 2, 2012).

6. Davy, H. *Phil. Trans. R. Soc. Lond.* **1814**, *104*, 74-93.

7. Gay-Lussac, J. *Ann. Chim.* **1813**, *88*, 311-318.

8. Courtois, B., *Ann. Chim.* **1813**, *88*, 304-310.

9. Swain, A. P. *Bull. Hist. Chem.* **2005**, *30*, 103-111.

10. Housecroft C. E.; Constable, E. C. *Chemistry*, 2nd ed.; Pearson Education Limited, Essex, UK, 2002.

11. Iodine. Wikipedia, the Free Encyclopedia. www.wikipedia.org (accessed Jul 3, 2012).

12. Saiz-Lopez, A.; Plane, J. M. C.; Baker, A. R.; Carpenter, L. J.; Von Glasow, R.; Gómez Martín, J. C.; McFiggans G.; Saunders, R. W.; *Chem. Rev.* **2012**, *112*, 1773-1804.

13. Zeng, Q.; He, Z.; San, X.; Ma, Y.; Tian, F.; Cui, T.; Liu, B.; Zou, G.; Mao, H.-K. *Proc. Natl. Acad. Sci. U. S. A.* **2008**, *105*, 4999-5001.

14. Usseglio, S.; Damin, A.; Scarano, D.; Bordiga, S.; Zecchina A.; Lamberti, C.; *J. Am. Chem. Soc.* **2007**, *129*, 2822-2828.

15. Guo, W.; Wang, D.; Hu, J.; Tang, Z. K.; Du, S.; *Appl. Phys. Lett.* **2011**, *98*, 043105.

16. Metrangolo, P.; Neukirch, H.; Pilati, T.; Resnati, G. *Acc. Chem. Res.* **2005**, *38,* 386-395.

17. Baxter, G. P. *J. Am. Chem. Soc.* **1907**, *29,* 127-136.

18. Van Bolhuis, F.; Koster, P. B.; Migchelsen, T. *Acta Crystallogr.* **1967**, *23,* 90-91.

19. Kobashi, K.; Etters, R. D. *J. Chem. Phys.* **1983**, *79,* 3018-3025.

20. Bondi, A. *J. Phys. Chem.* **1964**, *68,* 441-451.

21. Rowland, R. S.; Taylor, R. *J. Phys. Chem.* **1996**, *100,* 7384-7391.

22. Huber, K. P.; Herzberg, G. *Constants of Diatomic Molecules.* Van Nostrand Reinhold: New York, 1979.

23. English, C. A.; Venables, J. A. *Proc. R. Soc. London, Ser. A.* **1974**, *340,* 57-80.

24. Ibberson, R. M.; Moze O.; Petrillo, C. *Mol. Phys.* **1992**, *76,* 395-403.

25. Greenwood, N. N.; Earnshaw, A. *Chemistry of the Elements.* Elsevier: Amsterdam, 2006.

26. Atkins, P.; de Paula, J. *Atkins's Physical Chemistry.* 7th ed.; Oxford University Press: Oxford, UK, 2002.

27. Balchan, A. S.; Drickamer, H. G. *J. Chem. Phys.* **1961**, *34,* 1948-1949.

28. Takemura, K.; Fujii, Y.; Minomura, S.; Shimomura, O. *Solid State Commun.* **1979**, *30,* 137-139.

29. Steinteld, J. I.; Zare, R. N.; Jones, L.; Lesk M.; Klemperer, W. *J. Chem. Phys.* **1965**, *42,* 25-33.

30. Myer, J. A.; Samson, J. A. R. *J. Chem. Phys.* **1970**, *52,* 716-718.

31. Mulliken, R. S. *J. Chem. Phys.* **1971**, *55,* 288-309.

32. Donovan, R. J.; Macdonald, M. A.; Lawley, K. P.; Yencha, A. J.; Hopkirk, A. *Chem. Phys. Lett.* **1987**, *138,* 571-574.

33. Brand, J. C. D.; Hoy, A. R. *App. Spectrosc. Rev.* **1987**, *23,* 285-328.

34. Ridley, T.; Lawley, K. P.; Donovan, R. J. *J. Chem. Phys.* **2007**, *127,* 154306.

35. Scaria, A.; Namboodiri, V.; Konradi, J.; Materny, A. *Phys. Chem. Chem. Phys.* **2008**, *10,* 983-989.

36. Tellinghuisen, J. *J. Chem. Phys.* **2011**, *135*, 054301.

37. Li J.; Balasubramanian, K. *J. Mol. Spectrosc.* **1989**, *138*, 162-180.

38. De Jong, W. A.; Visscher, L.; Nieuwpoort, W. C. *J. Chem. Phys.* **1997**, *107*, 9046-9058.

39. Batista, V. S.; Coker, D. F. *J. Chem. Phys.* **1996**, *105*, 4033-4054.

40. National Institute of Standards and Technology. 'I', NIST Atomic Spectra Database Levels Data. www.nist.gov (accessed Jul 15, 2012).

41. Batista V. S.; Coker, D. F. *J. Chem. Phys.* **1997**, *106*, 6923-6941.

42. Yu, N.; Coker, D. F. *Mol. Phys.* **2004**, *102*, 1031-1044.

43. Hollas, J. M. *Modern Spectroscopy.* Wiley: West Sussex, UK, 2007.

44. Holzer, W.; Murphy, W. F.; Bernstein, H. J. *J. Chem. Phys.* **1970**, *52*, 399-407.

45. Magana, J. R.; Lannin, J. S. *Phys. Rev. B.* **1988**, *37*, 2475-2482.

46. Magana, J. R.; Lannin, J. S. *Phys. Rev. B.* **1985**, *32*, 3819-3823.

47. Anderson, A.; Sun, T. S. *Chem. Phys. Lett.* **1970**, *6*, 611-616.

48. Congeduti, A.; Nardone, M.; Postorino, P. *Chem. Phys.* **2000**, *256*, 117-123.

49. Helbing J.; M. Chergui, *J. Chem. Phys.* **2001**, *115*, 6158-6172.

50. Klein, M. L.; Venables, J. A., Eds. *Rare Gas Solids.* Academic Press: London, 1976.

51. Böhling, R.; Langen, J.; Schurath, U. *Chem. Phys.* **1989**, *130*, 419-432.

52. Li, Z.; Zadoyan, R.; Apkarian, V. A.; Martens, C. C. *J. Phys. Chem.* **1995**, *99*, 7453-7465.

53. Bargheer, M.; Gühr, M.; Schwentner, N. *J. Chem. Phys.* **2002**, *117*, 5-8.

54. Bihary, Z.; Gerber, R. B.; Apkarian, V. A. *J. Chem. Phys.* **2001**, *115*, 2695-2701.

55. Karavitis, M.; Apkarian, V. A. *J. Chem. Phys.* **2004**, *120*, 292-299.

56. Howard, W. F.; Andrews, L. *J. Raman Spectrosc.* **1974**, *2*, 447-462.

57. Macler, M.; Nicolai, J.-P.; Heaven, M. C. *J. Chem. Phys.* **1989**, *91*, 674-682.

58. Macler M.; Heaven, M. C. *Chem. Phys.* **1991**, *151*, 219-232.

59. Karavitis, M.; Zadoyan, R.; Apkarian, V. A. *J. Chem. Phys.* **2001**, *114*, 4131-4140.

60. Karavitis, M.; Kumada, T.; Goldschleger, I. U.; Apkarian, V. A. *Phys. Chem. Chem. Phys.* **2005**, *7*, 791-796.

61. Kiviniemi, T.; Aumanen, J.; Myllyperkiö, P.; Apkarian, V. A.; Pettersson, M. *J. Chem. Phys.* **2005**, *123*, 064509.

62. Amey, R. L.; Cole, R. H. *J. Chem. Phys.* **1964**, *40*, 146-148.

63. Beeken, P. B.; Hanson, E. A.; Flynn, G. W. *J. Chem. Phys.* **1982**, *78*, 5892-5899.

64. Grzybowski, J. M.; Andrews, L. *J. Raman Spectrosc.* **1975**, *4*, 99-113.

65. Bargheer, M.; Gühr, M.; Dietrich, P.; Schwentner, N. *Phys. Chem. Chem. Phys.* **2002**, *4*, 75-81.

66. Zadoyan, R.; Sterling, M.; Apkarian, V. A. *J. Chem. Soc., Faraday Trans.* **1996**, *92*, 1821-1829.

67. Onsager, L. *J. Am. Chem. Soc.* **1936**, *58*, 1486-1493.

68. Zadoyan, R.; Li, Z.; Martens, C. C.; Apkarian, V. A. *J. Chem. Phys.* **1994**, *101*, 6648-6657.

69. Benderskii, A. V.; Zadoyan, R.; Apkarian, V. A. *J. Chem. Phys.* **1997**, *107*, 8437-8445.

70. Bihary, Z.; Zadoyan, R.; Karavitis, M.; Apkarian, V. A. *J. Chem. Phys.* **2004**, *120*, 7576-7589.

71. Gühr, M.; Bargheer, M.; Dietrich, P.; Schwentner, N. *J. Phys. Chem. A.* **2002**, *106*, 12002-12011.

72. Bihary, Z.; Karavitis, M.; Apkarian, V. A. *J. Chem. Phys.* **2004**, *120*, 8144-8156.

73. Gühr, M.; Bargheer, M.; Fushitani, M.; Kiljunen, T.; Schwentner, N. *Phys. Chem. Chem. Phys.* **2007**, *9*, 779-801.

74. Segale, D.; Karavitis, M.; Fredj, E.; Apkarian, V. A. *J. Chem. Phys.* **2005**, *122*, 111104.

75. Segale, D.; Apkarian, V. A. *J. Chem. Phys.* **2011**, *135*, 024203.

76. Apkarian, V. A.; Schwentner, N. *Chem. Rev.* **1999**, *99*, 1509-1514.

77. Zadoyan, R.; Almy, J.; Apkarian, V. A. *Faraday Discuss.* **1997**, *108*, 255-269.

78. Gühr, M. *Coherent Dynamics of Small Molecules in Rare Gas Crystals.* PhD Thesis, Freien Universität Berlin, Cuvillier Verlag, Göttingen, 2005.

79. Karavitis, M.; Segale, D.; Bihary, Z.; Pettersson, M.; Apkarian, V. A. *Low Temp. Phys.* **2003**, *29*, 814-821.

80. Randall, K. L.; Donaldson, D. J. *Chem. Phys.* **1996**, *211*, 377-386.

81. Philippoz, J. M.; Van Den Bergh, H.; Monot, R. *J. Phys. Chem.* **1987**, *91*, 2545-2550.

82. Stevens Miller, A. E.; Chuang, C.-C.; Fu, H. C.; Higgins, K. J.; Klemperer, W. *J. Chem. Phys.* **1999**, *111*, 7844-7856.

83. Kubiak, G.; Fitch, P. S. H.; Wharton, L.; Levy, D. H. *J. Chem. Phys.* **1978**, *68*, 4477-4480.

84. Beswick, J. A.; Halberstadt, N.; Janda, K. C. *Chem. Phys.* **2012**, *399*, 4-16.

85. Kiviniemi, T.; Kiljunen, T.; Pettersson, M. *J. Chem. Phys.* **2006**, *125*, 164302.

86. Pakhira, S.; Das, A. K. *Theor. Chem Acc.* **2011**, *130*, 95-101.

87. Akopyan, M. E.; Lukashov, S. S.; Maslennikova, Y. D.; Poretsky, S. A.; Pravilov, A. M. *Chem. Phys.* **2009**, *362*, 27-33.

88. Lukashov, S. S.; Poretsky, S. A.; Pravilov, A. M. *Chem. Phys.* **2012**, *399*, 122-129.

89. Potter, E. D.; Herek, J. L.; Pedersen, S.; Liu, Q.; Zewail, A. H. *Nature.* **1992**, *355*, 66-68.

90. Tamres, M.; Duerksen, W. K.; Goodenow, J. M. *J. Phys. Chem.* **1968**, *72*, 966-970.

91. Passchier, A. A.; Gregory, N. W. *J. Phys. Chem.* **1968**, *72*, 2697-2702.

92. De Maine, P. A. D. *J. Chem. Phys.* **1956**, *24*, 1091-1093.

93. Keefer, R. M.; Allen, T. L. *J. Chem. Phys.* **1956**, *25*, 1059-1061.

94. Philippoz, J. M.; Melinon, P.; Monot, R.; van den Bergh, H. *Chem. Phys. Lett.* **1987**, *138*, 579-583.

95. Zhang, J.; Liu, X.; Gao, S.; Liu, Q.; Huang, B.; Dai, Y. *Int. J. Photoenergy* **2012**, *2012*, 536194.

96. Ye, J. T.; Tang, Z. K.; Siu, G. G. *App. Phys. Lett.* **2006**, *88*, 073114.

97. Ye, J. T.; Iwasa, Y.; Tang, Z. K. *Phys. Rev. B.* **2011**, *83*, 193409.

98. Van Der Marel, C.; Bras, W.; Van Der Lugt, W. *Mol. Phys.* **1988**, *64*, 445-456.

99. Andrews, L. *J. Am. Chem. Soc.* **1976**, *98*, 2152-2156.

100. Ault, B. S.; Andrews, L. *J. Mol. Spectrosc.* **1978**, *70*, 68-73.

101. Almy, J.; Kizer, K.; Zadoyan, R.; Apkarian, V. A. *J. Phys. Chem. A.* **2000**, *104*, 3508-3520.

102. Brust, M.; Walker, M.; Bethell, D.; Schiffrin, D. J.; Whyman, R. *J. Chem. Soc. Chem. Com.* **1994** 801-802.

103. Templeton, A. C.; Wuelfing, W. P.; Murray, R. W. *Acc. Chem. Res.* **2000**, *33*, 27-36.

104. Tsukuda, T. *Bull. Chem. Soc. Jpn.* **2012**, *85*, 151-168.

105. Ackerson, C. J.; Jadzinsky, P. D.; Kornberg, R. D. *J. Am. Chem. Soc.* **2005**, *127*, 6550-6551.

106. Jadzinsky, P. D.; Calero, G.; Ackerson, C. J.; Bushnell, D. A.; Kornberg, R. D. *Science.* **2007**, *318*, 430-433.

107. Walter, M.; Akola, J.; Lopez-Acevedo, O.; Jadzinsky, P. D.; Calero, G.; Ackerson, C. J.; Whetten, R. L.; Grönbeck, H.; Häkkinen, H. *Proc. Natl. Acad. Sci. U. S. A.* **2008**, *105*, 9157-9162.

108. Whetten, R. L.; Price, R. C. *Science.* **2007**, *318*, 407-408.

109. Häkkinen, H.; Walter, M.; Grönbeck, H. *J. Phys. Chem. B.* **2006**, *110*, 9927-9931.

110. Schnöckel, H.; Schnepf, A.; Whetten, R. L.; Schenk, C.; Henke, P. *Zeitschrift fur Anorganische und Allgemeine Chemie.* **2011**, *637*, 15-23.

111. Gao, Y.; Shao, N.; Zeng, X. C. *ACS Nano.* **2008**, 2, 1497-1503.

112. Reimers, J. R.; Wang, Y.; Cankurtaran, B. O.; Ford, M. J. *J. Am. Chem. Soc.* **2010**, *132*, 8378-8384.

113. Li, Y.; Galli, G.; Gygi, F. *ACS Nano.* **2008**, *2*, 1896-1902.

114. Han, Y.-K.; Kim, H.; Jung, J.; Choi, Y. C.; *J. Phys. Chem. C.* **2010**, *114*, 7548-7552.

115. Häkkinen, H. *Ligand-Protected Gold Nanoclusters as Superatoms – Insights from Theory and Computations,* in Johnston, R. J.; Wilcoxon, J.P., Eds. *Frontiers of Nanoscience,.* Elsevier, **2012**, *3*, 129-157.

116. Taylor, K. J.; Pettiette-Hall, C. L.; Cheshnovsky, O.; Smalley, R. E. *J. Chem. Phys.* **1992**, *96*, 3319-3329.

117. Heaven, M. W.; Dass, A.; White, P. S.; Holt, K. M.; Murray, R. W. *J. Am. Chem. Soc.* **2008**, *130*, 3754-3755.

118. Zhu, M.; Aikens, C. M.; Hollander, F. J.; Schatz, G. C.; Jin, R. *J. Am. Chem. Soc.* **2008**, *130*, 5883-5885.

119. Qian, H.; Y. Zhu; Jin, R. *Proc. Natl. Acad. Sci. U. S. A.* **2012**, *109*, 696-700.

120. Lopez-Acevedo, O.; Akola, J.; Whetten, R. L.; Grönbeck, H.; Häkkinen, H. *J. Phys. Chem. C.* **2009**, *113*, 5035-5038.

121. Levi-Kalisman, Y.; Jadzinsky, P. D.; Kalisman, N.; Tsunoyama, H.; Tsukuda, T.; Bushnell, D. A.; Kornberg, R. D. *J. Am. Chem. Soc.* **2011**, *133*, 2976-2982.

122. Mukamel, S. *Principles of Nonlinear Optical Spectroscopy.* Oxford University Press: New York, 1995.

123. Skinner, J. L. *Annu. Rev. Phys. Chem.* **1988**, *39*, 463-478.

124. Heller, E. J. *Acc. Chem. Res.* **1981**, *14*, 368-375.

125. Tannor, D. J. *Introduction to Quantum Mechanics – A Time-Dependent Perspective.* University Science Books: USA, 2007.

126. Ovchinnikov, M.; Apkarian, V. A. *J. Chem. Phys.* **1996**, *105*, 10312-10331.

127. Hamm, P.; Zanni, M. *Concepts and Methods of 2D Infrared Spectroscopy.* Cambridge University Press: Cambridge, UK, **2011**.

128. Ibrahim, H.; Gühr, M.; Schwentner, N. *J. Chem. Phys.* **2008**, *128*, 064504.

129. Pettersson, M.; Nieminen, J. *Chem. Phys. Lett.* **1998**, *283*, 1-6.

130. Rebane, K. K. *J. Luminesc.* **2002**, *100*, 219-232.

131. Moskovits, M.; Andrews, L. E., Eds. *Chemistry and Physics of Matrix-Isolated Species.* North-Holland Physics Publishing: Amsterdam, 1988.

132. Bondybey, V. E.; Bearder, S. S.; Fletcher, C. *J. Chem. Phys.* **1976**, *64,* 5243-5246.

133. Bondybey, V. E.; Fletcher, C. *J. Chem. Phys.* **1976**, *64,* 3615-3620.

134. Ovchinnikov, M.; Apkarian, V. A. *J. Chem. Phys.* **1998**, *108,* 2277-2284.

135. Whittle, E.; Dows, D. A.; Pimentel, G. C. *J. Chem. Phys.* **1954**, *22,* 1943.

136. Bondybey, V. E.; Smith, A. M.; Agreiter, J. *Chem. Rev.* **1996**, *96,* 2113-2134.

137. Himmel, H.-J.; Downs, A. J.; Greene, T. M. *Chem. Rev.* **2002**, *102,* 4191-4241.

138. Dunkin, I. R. *Matrix-Isolation Techniques – A Practical Approach.* Oxford University Press: New York, 1998.

139. Hulkko, E.; Lindgren, J.; Kiviniemi, T.; Pettersson, M.; Apkarian, V.A.; Kiljunen, T. Unpublished material.

140. Uotila, J. *Use of the Optical Cantilever Microphone in Photoacoustic Spectroscopy,* PhD Thesis, University of Turku, Annales Universitatis Turkuensis, Series AI, Part 395, 2009.

141. Xu, J.; Schwentner N.; Chergui, M. *J. Chem. Phys.* **1994**, *101,* 7381-7387.

142. Xu, J.; Schwentner, N.; Henning, S.; Chergui, M. *J. Chim. Phys.* **1995**, *92,* 541-565.

143. Jungwirth, P.; Fredj, E.; Gerber, R. B. *J. Chem. Phys.* **1996**, *104,* 9332-9339.

144. Helbing, J.; Chergui, M. *J. Luminesc.* **2001**, *94-95,* 611-616.

145. Hulkko, E.; Malola, S.; Häkkinen, H.; Engdahl, A.; Pettersson, M. Unpublished material.

146. Petroski, J.; Chou, M.; Creutz, C. *J. Organomet. Chem.* **2009**, *694,* 1138-1143.

ORIGINAL PAPERS

I

LONG-LIVED ELECTRONIC COHERENCE OF IODINE IN THE CONDENSED PHASE: SHARP ZERO-PHONON LINES IN THE B↔X ABSORPTION AND EMISSION OF I_2 IN SOLID Xe

by

Eero Hulkko, Johan Lindgren, Toni Kiljunen and Mika Pettersson, 2012

Journal of Physical Chemistry Letters **2012,** *3*, 1847-1852

https://doi.org/10.1021/jz300651v

II

ELECTRONIC SPECTROSCOPY OF I_2–Xe COMPLEXES IN SOLID KRYPTON

by

Eero Hulkko, Jussi Ahokas, Johan Lindgren, Pasi Myllyperkiö and Mika Pettersson,
2012

Journal of Chemical Physics **2012**, *136*, 174501

https://doi.org/10.1063/1.4706521

III

FROM MONOMER TO BULK: APPEARANCE OF THE STRUCTURAL MOTIF OF SOLID IODINE IN SMALL CLUSTERS

by

Eero Hulkko, Toni Kiljunen, Tiina Kiviniemi and Mika Pettersson, 2009

Journal of the American Chemical Society **2009**, *131*, 1050-1056

Reproduced with kind permission by
E. Hulkko, T. Kiljunen, T. Kiviniemi and M. Pettersson
Journal of the American Chemical Society **2009**, *131*, 1050-1056

https://doi.org/10.1021/ja806537u

IV

ELECTRONIC AND VIBRATIONAL SIGNATURES OF THE Au_{102}(p-MBA)$_{44}$ CLUSTER

by

Eero Hulkko, Olga Lopez-Acevedo, Jaakko Koivisto, Yael Levi-Kalisman,
Roger D. Kornberg, Mika Pettersson and Hannu Häkkinen, 2011

Journal of the American Chemical Society **2011**, *133*, 3752-3755

Reproduced with kind permission by
E. Hulkko, O. Lopez-Acevedo, J. Koivisto, Y. Levi-Kalisman,
R. D. Kornberg, M. Pettersson and H. Häkkinen
Journal of the American Chemical Society **2011**, *133*, 3752-3755

https://doi.org/10.1021/ja111077e